Targetome

ORIGINAL ARTICLE

Open Access

https://doi.org/10.48130/targetome-0026-0041

Targetome **2026**, 2(4): e039

KCC2 neuromodulation remodels metabolic and morphofunctional signatures across the neuromuscular axis in MDX mice

Alex D. Assis[1], Iola M. F. Duarte[2], Alessandra Sussulini[3] and Alexandre L. R. Oliveira[1*]

[1] *Institute of Biology, University of Campinas (UNICAMP), Campinas 13083-862, SP, Brazil*
[2] *CICECO – Aveiro Institute of Materials, Department of Chemistry, University of Aveiro, Aveiro 3810-193, Portugal*
[3] *Institute of Chemistry, University of Campinas (UNICAMP), Campinas 13083-970, SP, Brazil*
* Correspondence: alroliv@unicamp.br (Oliveira ALR)

Abstract

Duchenne muscular dystrophy is a hereditary neuromuscular disorder caused by dystrophin deficiency, leading to progressive muscle degeneration and weakness. Beyond muscle pathology, this condition is systemic and also affects central and peripheral nervous system function, promoting synaptic imbalance, metabolic alterations, and neuronal hyperexcitability. In this study, we investigated whether pharmacological modulation of chloride homeostasis using CLP290, a carbamate prodrug of CLP257, could restore synaptic, metabolic, and functional balance under dystrophic conditions. Four-week-old dystrophic mice and non-dystrophic controls received CLP290 10 mg·kg^{-1} *via* an intradermal biomembrane implant with controlled release for seven consecutive days. Motor performance was assessed using automated gait analysis, while molecular and cellular changes were evaluated by immunohistochemistry of lumbar spinal cord segments and protein expression analysis in skeletal muscle. Metabolic adaptations were examined using nuclear magnetic resonance-based metabolomics of neural tissues combined with liquid chromatography-mass spectrometry-based metabolomics of skeletal muscle. Treatment significantly improved gait stability, balance, and plantar contact dynamics without detectable toxic effects. Functional improvements were associated with increased expression of the neuronal potassium-chloride cotransporter and glutamate decarboxylase in presynaptic inputs to spinal alpha motor neurons, suggesting enhanced chloride regulation, strengthened inhibitory neurotransmission, and reduced neuronal excitability. Metabolomic analyses revealed coordinated metabolic remodeling in central and peripheral tissues, including bioenergetic adaptations in the spinal cord and partial normalization of dystrophic muscle metabolic profiles. Together, these findings support an integrated neural and metabolic mechanism underlying the functional benefits of the treatment and highlight its potential as an adjuvant strategy for early intervention in Duchenne muscular dystrophy.

Keywords: MDX mice, KCC2, Spinal cord, Muscular dystrophy

Citation: Assis AD, Duarte IMF, Sussulini A, Oliveira ALR. 2026. KCC2 neuromodulation remodels metabolic and morphofunctional signatures across the neuromuscular axis in MDX mice. *Targetome* 2(4): e039 https://doi.org/10.48130/targetome-0026-0041

Introduction

Duchenne Muscular Dystrophy (DMD)[1,2] is the most common and severe form of muscular dystrophy, with a prevalence of 7.1/100,000 male births, diagnosed between 4–7 years of age[3–6]. This pathology of recessive genetic origin is caused by X chromosome spontaneous mutations that affect the coding of the gene at the Xp21 locus, responsible for the synthesis of the 427 kDa cytoplasmic protein dystrophin, the largest isoform expressed in muscles and neuronal cells[7–9]. Due to different types of mutations, a genotype-phenotype pathological linkage can be observed in several variants of the DMD gene, leading to a myriad of functional impairments[10]. In DMD, the absence of functional dystrophin disrupts connections of the actin cytoskeleton to the extracellular matrix, destabilizing the myofibrils during contraction, inducing fragility and continuous loss of muscle fibers, with replacement of the myofibers by fibrotic tissue and infiltration of adipose tissue[11–13]. Molecular, structural, and functional dysfunctions caused by pathology, due to the absence of dystrophin, in muscle fibers have been extensively studied. However, comorbidities in the central (CNS) and peripheral (PNS) nervous system have been increasingly diagnosed in patients with DMD and MDX mice (an animal model for DMD)[14–17]. Nevertheless, studies evaluating the neuropathological effects of the mutation in dystrophin synthesis, which affects synaptic homeostasis in the spinal cord of DMD patients, are still scarce[18]. In MDX mice, there is evidence that spinal cord interneurons and alpha motoneurons are retrogradely affected by the muscle degeneration[19,20]. This, in turn, may affect the course of the disease, ultimately favoring skeletal muscle wasting[21,22].

The absence of dystrophin in the nervous system causes destabilization of postsynaptic GABA_A receptor clusters. This contributes to the cerebellar cortex's lack of neurofunctional control, which is due to the irregular firing of Purkinje cells. This irregular firing is caused by the reduction of GABA_A receptors, which compromises motor function in MDX mice[21,23,24]. Additionally, GABAA dysfunction in MDX mice has the potential to contribute to changes in neuronal excitability at central inhibitory synapses in neural regions lacking dystrophin, such as the hippocampus, amygdala, and sensory cortices[23,25–28]. In turn, the synthesis and release of gamma-aminobutyric acid (GABA) may be downregulated, resulting in disturbances and/or dysfunction of chloride influx and hyperexcitability[29]. In the post-synaptic neuron, Na/K/ATPase (NKCC1) and KCC2[30] contribute to the regulation of the membrane potential by modulating chloride levels intracellularly[31–33]. However, certain neuronal pathologies begin through neurodevelopmental disorders that have a genetic link to the loss of the KCC2 cotransporter, including autism, schizophrenia[34], and epilepsy[35]. By increasing the intracellular Cl- concentration[36–38], due to the negative regulation of KCC2, there is a decrease in rheobase, generating neuromuscular hyperexcitability in DMD patients and MDX mice[39–41].

Since KCC2 has critical functions at inhibitory synapses, its absence induces immediate death after birth in KCC2 knock-out mice, caused by loss of motor function, including respiratory suppression[42]. Thus, the depletion of the KCC2 cotransporter can be controlled by increasing its expression through the stimulation of pharmacological therapy with bioactive molecules such as CLP290[43,44]. This compound, derived from the CLP257 substrate, is improved due to carbamate protection and safer in relation to toxicological effects, indicating its therapeutic efficiency in clinical trials. Therefore, our hypothesis is based on the use of the prodrug CLP290, developed by Koninck et al. in partnership with the company Chlorion Pharma[45]. Designed as a modulator of chloride homeostasis via enhancement of KCC2 activity, this compound may contribute to the stabilization of neuronal excitability and neuromuscular function in DMD[46–50]. Despite increasing evidence that neuronal chloride regulation plays a critical role in synaptic stability and excitability, its contribution to neuromuscular dysfunction under dystrophic conditions remains incompletely understood. Therefore, the present study investigated whether pharmacological modulation of chloride homeostasis could mitigate neural, metabolic, and functional alterations associated with dystrophin deficiency. To address this question, we combined behavioral, molecular, and metabolomic approaches in a dystrophic mouse model.

Materials and methods

Animals

Mice of the C57BL/10 and dystrophic MDX strains (male, 4 weeks old, 15–20 g) were obtained from the Multidisciplinary Center for Biological Research of the University of Campinas (CEMIB/UNICAMP) and housed in the facilities of the Laboratory of Nerve Regeneration, Institute of Biology, UNICAMP. The animals were kept under a light-dark cycle (12 h/12 h) with controlled temperature and humidity and with water and pelleted food *ad libitum*. In total, 120 mice were required and are detailed in Table 1.

Drug treatment

The mice were anesthetized with isoflurane, using an inhalation anesthesia system for small rodents (BRASMED-Code 170130). The skin was carefully separated to accommodate GelMA/PCL microbandages, fabricated using the BIO X multimaterial system (BICO-Cellink, Gothenburg, Sweden). The models were designed in CAD (computer-aided design) and sliced in PrusaSlicer to generate the G-code, consisting of two flat-layer structures 10 mm × 10 mm in size and 0.5 mm in thickness. PCL/GelMA intradermal implantation included doses of 1, 5, and 10 mg·kg^{-1} of CLP290/β-cyclodextrin for 7 d, starting on the last day of the 4th week and ending on the last day of the 5th week of life. After surgery, the mice were kept in the animal house of the Laboratory of Nerve Regeneration (LRN) of the Department of Structural and Functional Biology of the Institute of Biology at Unicamp until the time of euthanasia. The intradermal PCL/GelMA biomembrane was designed as a sustained-release system to maintain continuous exposure to CLP290 throughout the treatment period *via* a single implantation, rather than as a tissue-targeted drug delivery platform.

Motor function tests and dose-response evaluation

The animals' spontaneous gait was evaluated to define the best responses after application of 1, 5, or 10 mg·kg^{-1}·d^{-1} of the prodrug CLP290. For that, the sciatic nerve functional index (SFI), posterior base of support, and maximum contact area were analyzed using an automated walking track test system (CatWalk XT System, Noldus Inc., Netherlands). This apparatus allows the animal to walk freely on a glass platform illuminated with green light, highlighting the footprints when the paws contact the path. Three runs were recorded by a high-speed camera placed under the walkway, and the data were analyzed by CatWalk XT 10.6 software (Noldus Inc.). The sciatic function index (SFI) was calculated according to the following formula (56): SFI = 118.9 ([ETS − NTS]/NTS) − 51.2 ([EPL − NPL]/NPL) − 7.5, where N, normal (right) side; E, experimental (left) side; PL, impression length; and TS, toe spread. For acclimatization, mice were individually placed in the system to walk for 5 min·d^{-1} for 4 d before the start of the experiments. The runs were acquired every day for seven consecutive days at the same time, keeping the environmental conditions standardized, and the data were collected from each animal per group. Run durations between 0.50 and 5.00 at a maximum speed with a variation of 60% were considered compliant. The camera gain was set to 25.01 and the detection threshold to 0.25. Four compatible runs were acquired per trial.

Collection and preparation of tissues

After the 7-d treatment period with CLP290 or vehicle, the mice were anesthetized with an overdose of xylazine (30 mg·kg^{-1}) and ketamine (300 mg·kg^{-1}) and underwent thoracotomy followed by transcardiac perfusion with 0.1 mol·L^{-1} sodium phosphate-buffered saline (PBS, with 0.9% NaCl; pH 7.38). Next, we extracted the tibialis anterior muscles for Western blotting analysis. The mice designated for spontaneous locomotion tests were the same used for immunohistochemical analyses. In addition to the saline solution, transcardiac perfusion was performed with fixative solution (4% paraformaldehyde in 0.1 mol·L^{-1} PBS). After fixation, the lumbar spinal cords and DRG were dissected and immersed in the same fixative solution overnight at 4 °C. Subsequently, the specimens were washed three times with 0.1 mol·L^{-1} PBS, then immersed in a series of sucrose solutions (10%, 20% and 30%, 24 h each). Samples were embedded in Tissue-Tek, frozen in n-hexane at a controlled temperature (−25 to −30 °C) and then cryostat sectioned or stored at −20 °C.

Tissue collection for NMR and LC-MS

Mice were anesthetized with an overdose of xylazine (30 mg·kg^{-1}) and ketamine (300 mg·kg^{-1}). A thoracotomy was performed, followed by cardiac puncture to collect 0.8–1.0 mL of blood, which

Table 1. Experimental groups, mouse strains, treatments, and evaluation methos used throughout the study.

Groups	Catwalk analysis	Immuno histochemistry	Western blotting	NMR	Metabolomics
C57BL/10JUnib-Vehicle	6	5*	6*	6	6
C57BL/10Unib-CLP290	18§	6*	5*	6	6
C57BL/10-Dmd<mdx>/PasUnib-Vehicle	6	6*	6*	6	6
C57BL/10-Dmd<mdx>/PasUni-CLP257	18§	6*	6*	6	6

§ Two groups with (n = 18) and two groups with (n = 6), tested at doses of 1, 5, and 10 mg·kg^{-1}. * The same mice were used for the different techniques.

was processed for plasma separation using 3.2% citrate (9:1 ratio) and centrifuged at 3,000 × g for 10 min at 4 °C under nitrogen. In a separate cohort, animals underwent transcardiac perfusion with 0.1 mol·L^{-1} sodium phosphate-buffered saline (PBS; 0.9% NaCl, pH 7.38). Subsequently, the tibialis anterior muscles, sciatic nerves, and lumbar spinal cords were harvested, immediately snap-frozen in liquid nitrogen, and stored in a −80 °C ultrafreezer until analysis.

Western blotting of the tibialis anterior muscles

The Western blotting method used to quantify dystrophin protein in tibialis anterior muscles was previously described by Mizobuti et al.[51]. Briefly, total protein determination was performed using the Bradford method[52]. Fifty micrograms of total protein homogenate were loaded on 15% SDS-polyacrylamide gels. Immediately after electrophoresis, the proteins were transferred to nitrocellulose membranes and probed with their respective primary dystrophin antibody (Invitrogen PA589628). Subsequently, the membranes were incubated with anti-rabbit secondary antibody (Promega Corporation W4011). Additionally, to control for protein loading, transfer, and nonspecific variations in protein quantification, blots were stripped and re-probed for β-actin. We used ImageJ software to determine the pixel intensities of each band.

Immunohistochemistry

Transverse sections of the lumbar spinal cord and dorsal root ganglia (DRG), 12 μm thick, were acquired using a cryostat (Leica CM, 1860). Subsequently, the sectioned tissues were transferred to gelatinized glass slides and stored at −20 °C until use. The slides were then selected and acclimatized at room temperature, and the sections were outlined with a hydrophobic pen (PAP pen, Sigma Z377821). The slides were transferred to a humid chamber that protects photosensitive reagents from light. The sections were immersed in 0.01 M PBS (3 × 5 min each), lightly dried on the periphery of the slide, and incubated with 150 μL of blocking solution (3% bovine serum albumin in 0.1 mol·L^{-1} PBS) for 45 min. Subsequently, the primary antibodies in Table 2 were diluted in incubation solution (1.5% bovine serum albumin and 0.2% Tween in 0.1 mol·L^{-1} PBS), and 100 μL was applied to each slide/section and incubated overnight in the refrigerator. After the primary antibody incubation period, sections were washed with 0.01 mol·L^{-1} PBS and incubated with the appropriate secondary antibody for 45 min. The sections were again washed with 0.01 mol·L^{-1} PBS and coverslipped with glycerin/PBS (3:1). The slides/tissues were observed with an epifluorescence microscope (Leica DMB5500) and documented with a digital camera (Leica DFC 345 FX), using specific filters according to the secondary antibodies. For quantification, three images of tissue sections from each animal in each experimental group were selected. Integrated pixel density, which represents the intensity of antibody bound to the protein of interest, was measured from transverse sections of the lumbar spinal cord. We used the IMAGEJ software (v1.33u, National Institutes of Health, USA). For each lumbar spinal cord, the mean ± standard error of the mean of each experimental group was calculated and, using these values, comparisons were made between the groups.

Table 2. Primary antibodies used for immunohistochemistry and Western blotting analysis.

Antibody/neurotoxin	Manufacturer	Host	Cat. number	Concentration
KCC2	Millipore	Rabbit	07-432	1:500
VGLUT1	Synaptic systems	Rabbit	135,303	1:1,000
GAD65	Abcam	Mouse	ab26113	1:750
AMPA	Abcam	Rabbit	ab31232	1:750
CHAT	Abcam	Sheep	Ab18736	1:500
GFAP	Abcam	Rabbit	ab7260	1:1,000
DYSTROPHIN§	Invitrogen	Rabbit	PA589628	1:1,000

§ Antibody used for Western blotting.

NMR-metabolomics of lumbar spinal cord and sciatic nerve

Metabolite extraction

Frozen segments of lumbar spinal cord from L4 to L6 and sciatic nerves of mice were weighed. Subsequently, the tissues in 2 mL cryovials were homogenized for 40 s with a Polytron PT-MR 1600 E homogenizer (Kinematica AG) in a ratio of ≤ 50 mg of spinal cord and ≤ 17 mg of nerves to 1 mL of cold 100 mmol·L^{-1} phosphate buffer, pH 7.4. After tissue homogenization, metabolites were extracted using methanol : chloroform : milliQ water (2:2:0.5), as previously described[53,54]. The aqueous and organic extracts were vacuum dried (SpeedVac, Eppendorf), and all dried extracts were subsequently stored at −80 °C.

Spectral acquisition

Polar extracts were reconstituted in 200 μL of deuterated phosphate buffer (100 mmol·L^{-1}, pH 7.4) containing 0.2 mmol·L^{-1} TSP-d_4 (3-trimethylsilyl-2,2,3,3-d_4-propionate sodium salt) and transferred to 3 mm NMR tubes. Spectra were acquired at 298 K on a 500 MHz ^{1}H NMR spectrometer (Bruker Avance III HD, Portuguese NMR network) equipped with a cryoprobe. Standard one-dimensional (1D) ^{1}H spectra were recorded with a spectral width of 7,002.80 Hz, a recycle time of 5 s, and 128 scans, using the 'noesypr1d' pulse sequence. To confirm spectral assignments, two-dimensional ^{1}H-^{1}H TOCSY and *J*-resolved spectra were acquired for selected samples.

Data processing and acquisition

Spectra were processed in TopSpin 4.1 (Bruker) with exponential apodization (0.3 line broadening), manual phasing, baseline correction, and calibration to the TSP signal at δ 0.00 ppm. Metabolite assignment was based on matching 1D ^{1}H spectral data to reference spectra available in Chenomx (Edmonton, Canada) and BBIOREFCODE (Bruker BioSpin, Rheinstetten, Germany). Metabolite quantification was performed using signal deconvolution and fitting to reference spectra from the Chenomx library through the Profiler module of Chenomx NMR Suite v10.1 Professional.

LC-MS-based metabolomics of skeletal muscle

Sample collection and storage

Tibialis anterior (TA) muscles were collected from C57BL/10 (BL) and MDX mice, including control and CLP290-treated groups (n = 6 per group). Muscles were carefully dissected, rapidly frozen to arrest metabolic activity, and stored at −80 °C until metabolite extraction.

Metabolite extraction

Metabolite extraction was performed under cold conditions using using 400 μL of MeOH/H_2O (70:30, *V/V*), suitable for untargeted metabolomics. Muscle samples were homogenized, followed by centrifugation to remove insoluble material. The resulting supernatant was collected for LC-MS analysis. Extraction blanks (BLANK), consisting of empty tubes processed alongside the biological samples, were included to monitor potential contamination and background signals introduced during sample preparation.

UHPLC-MS analysis

Metabolomic analyses were carried out using an UltiMate 3000 UHPLC system coupled to a Q Exactive Orbitrap mass spectrometer. Data were acquired in separate analytical runs using positive (ESI$^+$)

and negative (ESI^-) electrospray ionization modes. Chromatographic separation was achieved on an ACQUITY BEH C18 column (2.1 mm × 50 mm, 1.7 μm), maintained at 55 °C, with a flow rate of 0.4 mL·min^{-1} and an injection volume of 5 μL. Mobile phase A consisted of ACN : H_2O (60:40, *V/V*) containing 1 mmol·L^{-1} ammonium formate and 0.1% formic acid, while mobile phase B consisted of IPA : ACN (90:10, *V/V*) with the same additives. The gradient elution was applied over a total run time of 25 min, including elution, re-equilibration, and column stabilization steps.

Mass spectrometry data acquisition

Mass spectrometric data were acquired in full-scan mode (MS1) over an *m/z* range of 100–1,500, using a resolution of 70,000 (at *m/z* 200), an automatic gain control (AGC) target of 3×10^6 ions, and a maximum injection time of 200 ms.

Quality control samples

Analytical stability and reproducibility were monitored using quality control (QC) samples prepared as a pooled mixture containing aliquots from all biological samples. QC samples were injected periodically throughout the analytical sequence to assess instrument performance and data consistency.

Data processing

Raw LC-MS data were processed using MSConvert followed by MZmine, following a standard untargeted metabolomics workflow, including mass detection, chromatogram construction, chromatographic deconvolution, isotopic peak grouping, and feature alignment across samples. Missing values arising from stochastic MS detection were addressed by applying gap filling after feature alignment, ensuring consistent feature intensity estimation across the dataset. Feature quality control was performed using the Feature List Rows Filter module. Features containing MS/MS information were explicitly preserved by enabling the 'Feature with MS2 scan' and 'Never remove features with MS2' options, prioritizing structurally informative variables. Following filtering, feature intensity normalization was applied within MZmine to the filtered, aligned, and gap-filled feature list to correct for systematic analytical variability. This procedure generated the final normalized feature intensity matrix defined by *m/z*-retention time pairs. The normalized dataset was subsequently analyzed using MetaboAnalyst and RStudio. Multivariate analysis was performed using Principal Component Analysis (PCA), and group comparisons were conducted using the non-parametric Kruskal–Wallis test. Significant metabolic features were visualized using heatmaps and volcano plots.

Statistical analysis

All quantitative data are presented as mean ± standard error of the mean (SEM), with * $P < 0.05$ considered statistically significant. Conventional experimental data were analyzed using GraphPad Prism (v8.0.1; GraphPad Software, USA). Group comparisons for immunohistochemistry and functional recovery were performed using one-way analysis of variance (ANOVA) followed by Tukey's multiple comparisons test.

Table 3. Functional improvement with CLP290 treatment, 10 mg/kg/d, during the 4th week of life of dystrophic MDX mice and C57BL/10 controls.

Assay CatWalk	Groups			
	BLVehicle	MDXVehicle	BLCLP290	MDXCLP290
Base of support	3.30 ± 0.03	3.30 ± 0.06	2.90 ± 0.03	3.00 ± 0.03
Max contact area left	0.42 ± 0.01	0.45 ± 0.01	0.30 ± 0.01	0.36 ± 0.01
Max contact area right	0.41 ± 0.01	0.41 ± 0.01	0.30 ± 0.01	0.33 ± 0.01

For LC-MS-based metabolomics, analyses were conducted separately for positive and negative ionization modes. Principal component analysis (PCA) was used for exploratory assessment of global metabolic variation and sample clustering. Univariate differences between groups were evaluated using the non-parametric Kruskal–Wallis test. The 25 most significant features were visualized using heatmaps following $\log_2$ transformation and feature-wise autoscaling (*z*-score), including QC and blank samples. The six most discriminant features were further examined using boxplots, with Dunn's post hoc test applied for pairwise comparisons.

Results

Functional adaptation of spontaneous gait in MDX mice during treatment with CLP290 (10 mg·kg^{-1})

The locomotor performance of the experimental groups was evaluated by the spontaneous walking track test (CatWalk system). Thus, data were acquired every day, for a period of 7 d, totaling 48 measurements per group, from the 4th week of age in both strains (Table 3). We analyzed the posterior base of support and the maximum right and left contact area (Fig. 1). The posterior base of support (BOS) is the average width between the hind limbs, which implicitly represents balance. We observed that C57BL10 and MDX animals, when treated with 1 and 10 mg·kg^{-1} of CLP290, reduced their posterior support measures in the BOS (**** $P < 0.0001$ and ** $P < 0.01$) compared to the measures of C57BL10 and MDX vehicles, in the 4th week. Furthermore, treatment with CLP290 10 mmg·kg^{-1}, in the MDX and C57BL/10 strains, resulted in less dispersion of BOS measurements between the animals in each group, demonstrated in the dotted lines in Fig. 1a. The analysis of the maximum contact area of the left and right footprints in contact with the glass plate (Fig. 1b and c) demonstrated that the treatment with CLP290 10 mg/kg, in the MDX and C57BL/10 lines, reduced the area of the footprints in maximum contact with the glass platform in relation to the vehicle controls (**** $P < 0.0001$; Table 3).

Intradermal implants containing CLP290 (10 mg·kg^{-1}) did not alter 427 KDa dystrophin expression in the tibial anterior muscle of MDX mice

After seven consecutive days of treatment with CLP290 (10 mg·kg^{-1}·d^{-1}) or the β-cyclodextrin vehicle, the presence or absence of the total 427 kDa dystrophin protein in the anterior tibial muscles of C57BL/10 control mice and MDX dystrophic mice was evaluated by Western blotting (Supplementary Table S1). A minimal 427 kDa dystrophin signal band was observed in vehicle- and CLP290-treated MDX mice compared with their respective vehicle-treated C57BL/10 controls (C57BL/10, 12.56 ± 1.67 and MDX, 0.81 ± 0.72, **** $P < 0.0001$; Supplementary Fig. S1) and CLP290-treated counterparts (C57BL/10, 13.69 ± 0.94 and MDX, 0.39 ± 0.15, **** $P < 0.0001$; Fig. 2a), consistent with the expected dystrophin levels. Ponceau S staining was used for visual inspection of transfer efficiency[55,56].

Treatment with CLP290 enhances KCC2 expression in lumbar spinal motoneurons of MDX mice

After seven uninterrupted days of treatment with CLP290 10 mg·kg^{-1}·d^{-1} or β-cyclodextrin vehicle, the immunoreactivity for chloride cotransporter coverage, anti-KCC2, obtained from the motor nucleus in the lamina IX of Rexed, resulted in reduced levels of

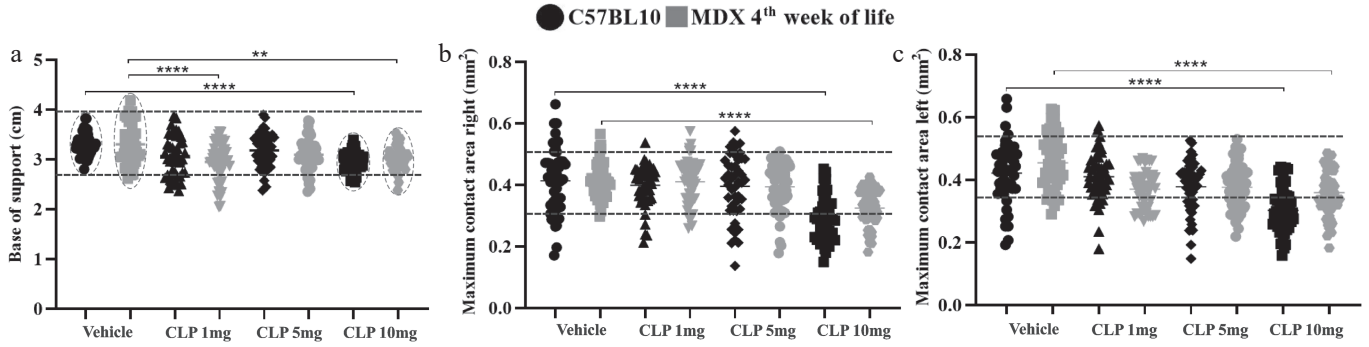

Fig. 1 (a) Posterior base of support; (b) left maximum contact area; and (c) right maximum contact area in C57BL/10 and MDX dystrophic mice following treatment with the prodrug CLP290. Statistical significance: ** $P < 0.01$, **** $P < 0.0001$. Data are presented as mean ± SEM, $n = 6$, and locomotor parameters were recorded repeatedly throughout the 7-day treatment period.

anti-KCC2 expression (Supplementary Table S1), in the vehicle dystrophic line, compared to the vehicle C57BL/10 counterpart (*** $P < 0.001$; Fig. 2a and b). Furthermore, we observed a trend toward reduced immunoreactivity in the plasma membrane of motoneurons from MDX vehicle mice (Fig. 2a and b). Also, after treatment with 10 mg·kg^{-1} of CLP290, a more intense KCC2 expression in treated MDX mice can be seen, compared with the control C57BL/10 counterpart (*** $P < 0.001$; Fig. 2a–d). This is also true when compared with the vehicle dystrophic line (**** $P < 0.0001$; Fig. 2b–d). In addition to the motor nucleus, collectively, the treatment optimized KCC2 labeling, increasing its expression in the plasma membrane of motoneurons of MDX mice, compared with C57BL/10 and MDX vehicles (* $P < 0.05$; Fig. 2a–d, and *** $P < 0.001$; Fig. 2b–d, respectively). Figure 3e and f present quantitative data regarding integrated pixel density. In parallel with these changes in chloride homeostasis-related signaling, a significant reduction of GAD65 expression in vehicle MDX mice compared to the control C57BL/10 strain (** $P < 0.01$; Fig. 2g and h) was observed. However, following treatment with 10 mg/kg of CLP290, there was upregulation of GAD65 in lamina IX of both C57BL/10 and MDX mice, compared to their vehicle counterparts (* $P < 0.05$, ** $P < 0.01$; Fig. 2h–j). Figures 2j and k present quantitative data regarding integrated pixel density.

The immunoreactivity for the vesicular glutamatergic vesicles (VGLUT1), in cross-sections of the lumbar spinal cord, first observed in the panoramic view of the gray matter, shows a tendency for

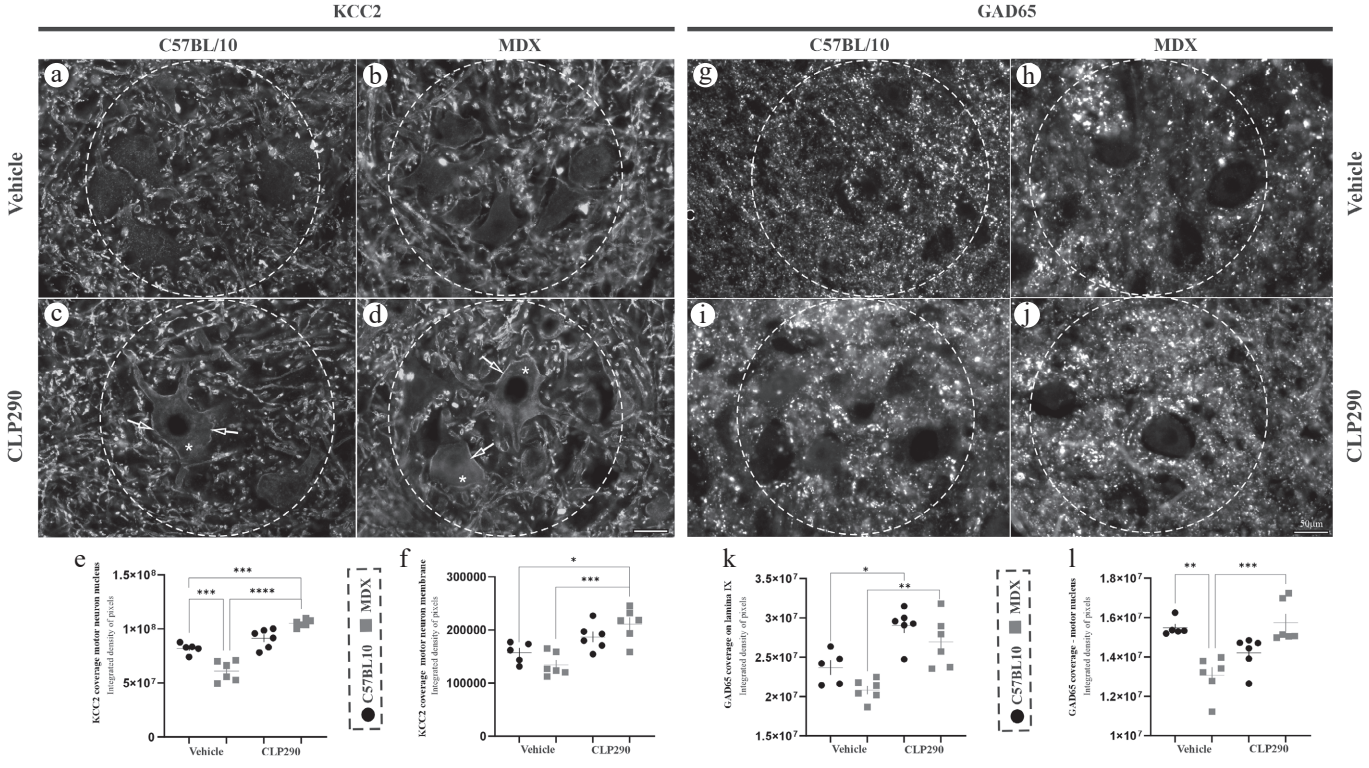

Fig. 2 (a)–(f) Anti-KCC2 immunostaining of lumbar spinal cord cross sections, showing increased staining intensity after 7 d of CLP290 treatment. (a)–(c) C57BL/10; (b)–(d) MDX; (e), (f) quantification of integrated pixel density and statistical significance of intergroup comparisons (*** $P < 0.001$; **** $P < 0.0001$). Motor nucleus (dotted circle), motoneuron plasma membrane (arrows), and motoneuron cytoplasm (*) exhibiting positive staining. (g)–(l) Anti-GAD65 immunostaining of lumbar spinal cord cross sections, showing increased staining intensity after 7 d of CLP290 treatment. (g)–(i) C57BL/10; (h)–(j) MDX. (k), (l) Quantification of integrated pixel density and statistical significance of intergroup comparisons (* $P < 0.05$; ** $P < 0.01$; *** $P < 0.001$). Rexed lamina IX and motoneuron nucleus (dotted circles). Scale bar: 50 µm. Data are presented as mean ± SEM, $n = 6$. Quantitative analyses were performed from multiple lumbar spinal cord sections containing motoneurons from each animal, as described in the Methods section.

https://doi.org/10.48130/targetome-0026-0041

MDX mice to exhibit greater VGLUT1 labeling than the C57BL/10 control (Fig. 3; Supplementary Table S1). Interestingly, CLP290 treatment reduced VGLUT1 expression in both MDX and C57BL/10 mice (* $P < 0.05$; *** $P < 0.001$; **** $P < 0.0001$; Fig. 3c and d). Figure 3e–g presents the quantitative data referring to integrated pixel density. Converging with these treatment-related alterations in excitatory synaptic markers, anti-GFAP (glial fibrillary acidic protein) immunohistochemistry, an astrocytic marker, revealed elevated expression in Rexed lamina IX of MDX vehicle mice compared to the C57BL/10 vehicle counterpart (** $P < 0.01$; Fig. 3h and i). Treatment with CLP290 (10 mg·kg^{-1}) significantly reduced GFAP expression in the dystrophic strain compared to the MDX vehicle group (*** $P < 0.001$; Fig. 3i–k). Furthermore, MDX mice treated with CLP290 showed no statistical difference in GFAP expression compared to the C57BL/10 group. Figure 3l presents the quantitative analysis regarding integrated pixel density.

The immunoreactivity for coverage of the α-Amino-3-hydroxy-5-methyl-4-isoxazole-propionic acid receptor (AMPAr), a subtype of ionotropic glutamate receptor[57], revealed that treatment with 10 mg·kg^{-1} of CLP290 significantly downregulates its expression in the dystrophic strain compared to the C57BL/10 vehicle and MDX vehicle groups, respectively (* $P < 0.05$, **** $P < 0.0001$; Fig. 4a–d). Figure 4e presents the quantitative integrated pixel density data. Complementing these alterations observed in glutamatergic signaling components, immunoreactivity for choline acetyltransferase (ChAT) coverage, used to identify cholinergic neurons[58], indicates increased expression in the soma and plasma membrane of motoneurons (Supplementary Fig. S1) in MDX mice compared to the control strain C57BL/10 (* $P < 0.05$; Fig. 4f and g). However, reduced ChAT expression in the motoneuron soma was observed in both MDX and C57BL/10 mice following CLP290 treatment (** $P < 0.01$, **** $P < 0.0001$; Fig. 4h and i). Furthermore, the treatment reduced anti-ChAT expression in the plasma membrane of motoneurons from MDX mice compared to treated C57BL/10 mice (** $P < 0.01$; Fig. 4h and i). Figure 4j presents the quantitative data regarding integrated pixel density.

NMR-metabolomics

Metabolic profile of the lumbar spinal cord in response to CLP290 treatment

NMR analyses of lumbar spinal cord extracts made it possible to identify 23 polar metabolites, including organic acids (4-aminobutyrate [GABA], acetate, aspartate, citrate, formate, fumarate, glutamate, lactate, N-acetylaspartate, and succinate)[59–63]; amino acids and related compounds (alanine, aspartate, glutamate, glutamine, glycine, taurine, creatine, and creatine phosphate)[64,65]; choline-containing and other quaternary ammonium metabolites (choline, O-phosphocholine, sn-glycero-3-phosphocholine, and carnitine); polyols (glycerol and myo-inositol)[66,67]; and a nucleoside derivative (S-adenosylhomocysteine, SAH)[68]. These metabolites were then quantified by NMR in the four groups compared (BLvehicle, MDX-vehicle, BLCLP290, and MDXCLP290) and their levels expressed as nmol·mg^{-1} of tissue. Their variations are discussed in the following sections.

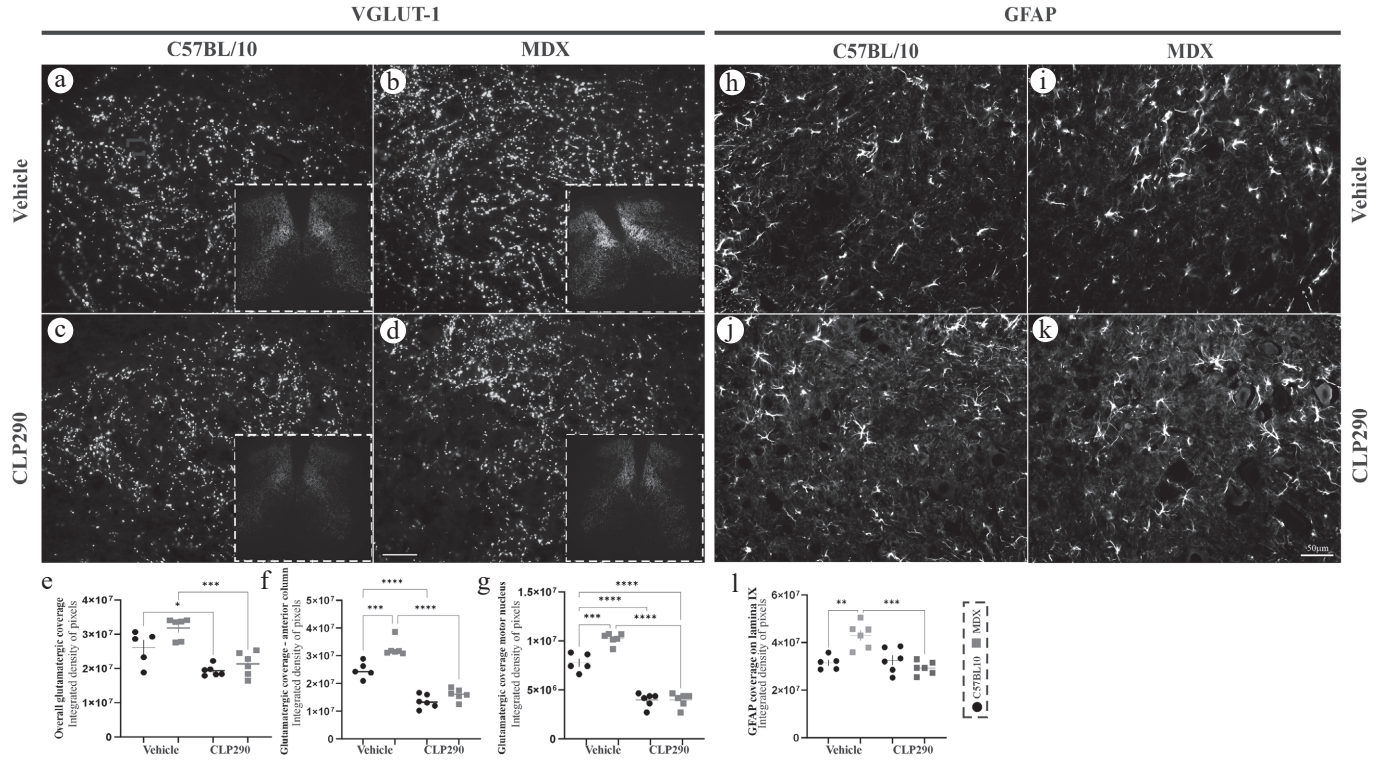

Fig. 3 (a)–(g) Anti-VGLUT1 immunohistochemistry of transverse sections of the lumbar spinal cord, showing reduced staining intensity after CLP290 administration. (e)–(g) Quantification of integrated pixel density and statistical significance of intergroup comparisons (* $P < 0.05$; *** $P < 0.001$; **** $P < 0.0001$). Scale bar: 50 µm. (h)–(l) Anti-GFAP (glial fibrillary acidic protein) immunohistochemistry, an astrocytic marker, revealed elevated expression in Rexed lamina IX of MDX vehicle mice compared to C57BL/10 vehicle controls (** $P < 0.01$; [h], [i]). Treatment with CLP290 (10 mg·kg^{-1}) significantly reduced GFAP expression in MDX mice compared to the MDX vehicle group (*** $P < 0.001$; [i]–[k]). No statistically significant difference was observed between CLP290-treated MDX mice and the C57BL/10 group. (l) Quantification of integrated pixel density. Data are presented as mean ± SEM, $n = 6$. Quantitative analyses were performed from multiple lumbar spinal cord sections containing motoneurons from each animal, as described in the Methods section. Scale bar: 50 µm.

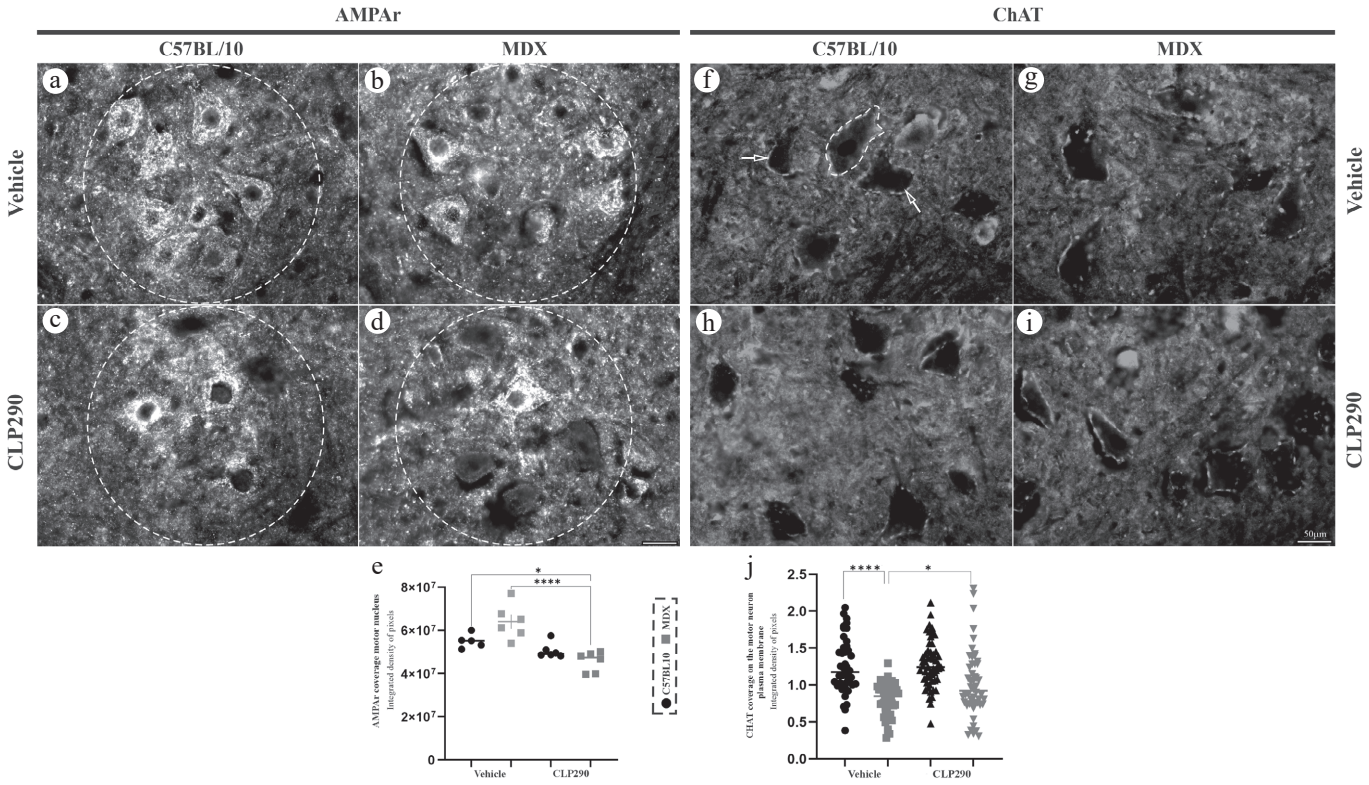

Fig. 4 (a)–(e) Anti-AMPAr immunostaining of lumbar spinal cord transverse sections showing reduced staining intensity in the motor nucleus of MDX mice after CLP290 treatment. (e) Quantification of integrated pixel density and statistical significance of intergroup comparisons (* $P < 0.05$; **** $P < 0.0001$). (f)–(j) Anti-ChAT immunostaining revealing increased motoneuron plasma membrane coverage (arrows) in MDX mice after CLP290 treatment. (j) Quantification of integrated pixel density of presynaptic ChAT+ membrane coverage and statistical significance of intergroup comparisons (* $P < 0.05$). Data are presented as mean ± SEM, $n = 6$. Quantitative analyses were performed from multiple lumbar spinal cord sections containing motoneurons from each animal, as described in the Methods section. Scale bar: 50 µm.

Energy and phosphorylation

After seven consecutive days of treatment with CLP290 (10 mg·kg^{-1}·d^{-1}) or β-cyclodextrin vehicle, metabolite concentrations in the lumbar spinal cord were quantified by NMR and expressed as nmol·mg^{-1} of tissue (Fig. 5). With respect to energy metabolism and phosphorylation-related compounds, CLP290 treatment in C57BL/10 mice was associated with higher levels of creatine, lactate, and N-acetylaspartate compared with vehicle-treated controls (no statistical difference; Fig. 5a, f, and h). In MDX mice, CLP290 treatment resulted in significant differences in creatine, creatine phosphate, lactate, and N-acetylaspartate relative to vehicle-treated MDX mice (* $P < 0.05$; Fig. 5a, b, f, and h). Succinate and fumarate concentrations were increased following CLP290 treatment in MDX mice and in both genotypes, respectively; however, these changes did not reach statistical significance (Fig. 5c and d), while no significant differences were detected for citrate or formate in either genotype (Fig. 5e and g).

Osmoregulation and membranes

In addition to these metabolic adjustments associated with cellular energy buffering, we next examined metabolites related to osmoregulation and membrane dynamics. CLP290 treatment was associated with increased concentrations of myo-inositol and carnitine in MDX-CLP290 mice compared with C57BL/10 vehicle-treated controls (** $P < 0.01$; Fig. 5i and n). Choline and O-phosphocholine levels showed an upward trend following CLP290 treatment in both genotypes, although these changes did not reach statistical significance (Fig. 5j and k). Glycerol concentrations were not significantly altered by CLP290 treatment in either genotype (Fig. 5l). A significant increase in glycerophosphocholine (GPC) concentration was observed in C57BL/10 mice treated with CLP290 compared with vehicle-treated controls (* $P < 0.05$), whereas no significant difference was detected in MDX mice (Fig. 5m).

Excitatory and inhibitory amino acids

Considering that membrane turnover and osmotic regulation are tightly coupled to neurotransmitter cycling and amino acid homeostasis, we subsequently evaluated excitatory and inhibitory amino acids. CLP290 treatment was associated with significant increases in glutamate, aspartate, and 4-aminobutyrate concentrations in both C57BL/10 and MDX mice compared with their respective vehicle-treated controls, with statistically significant differences observed in MDX-CLP290 mice compared with C57BL/10 vehicle-treated mice (* $P < 0.05$ or ** $P < 0.01$; Fig. 5o–q). Significant increases in glycine and taurine concentrations were also observed following CLP290 treatment in both genotypes, again with statistically significant differences in MDX-CLP290 mice compared with C57BL/10 vehicle-treated mice (* $P < 0.05$; Fig. 5s and t), while alanine concentrations were not significantly altered by CLP290 treatment in either genotype (Fig. 5r).

Nitrogen metabolism and methylation

Finally, to determine whether these metabolic adaptations extended to nitrogen metabolism and methylation-related pathways, we quantified metabolites associated with these processes. CLP290 treatment did not result in statistically significant changes in S-adenosylhomocysteine or acetate concentrations in either C57BL/10 or MDX mice (Fig. 5u and w), and glutamine levels were likewise not altered following CLP290 treatment (Fig. 5v).

https://doi.org/10.48130/targetome-0026-0041

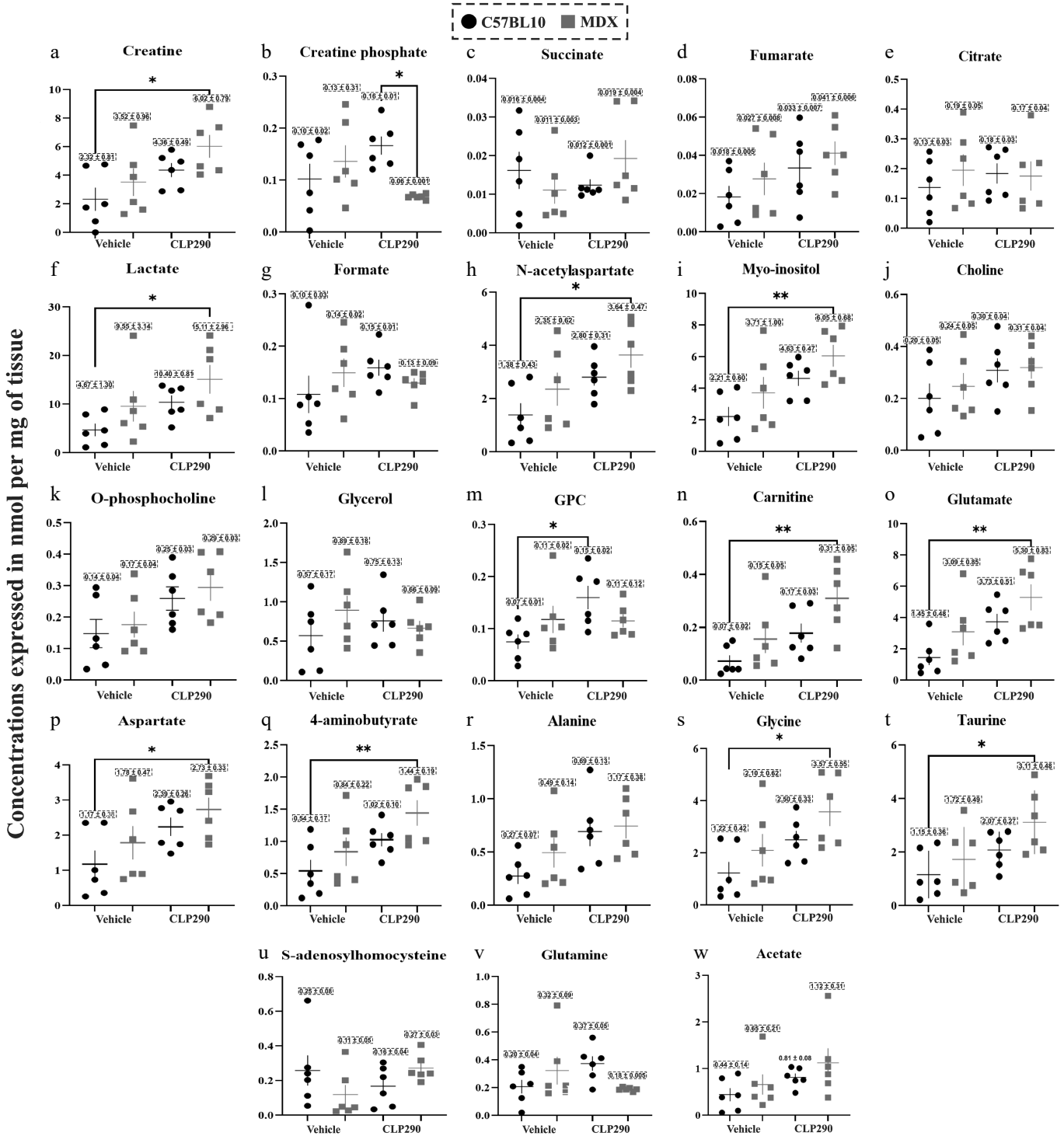

Fig. 5 Quantitative NMR-based analysis of lumbar spinal cord metabolites, expressed as nmol·mg^{-1} of tissue, in C57BL/10 and MDX mice treated with vehicle or CLP290 for 7 d. (a)–(h) Energy and phosphorylation-related metabolites: (a) creatine, (b) creatine phosphate, (c) succinate, (d) fumarate, (e) citrate, (f) lactate, (g) formate, and (h) N-acetylaspartate. Significant differences between MDX–CLP290 and C57BL/10 vehicle groups were observed for (a) creatine, (f) lactate, and (h) N-acetylaspartate. (c) Succinate and (d) fumarate increased without reaching statistical significance; (e) citrate and (g) formate were unchanged. (i)–(n) Osmoregulation and membrane-related metabolites: (i) myo-inositol, (j) choline, (k) O-phosphocholine, (l) glycerol, (m) glycerophosphocholine (GPC), and (n) carnitine. CLP290 increased (i) myo-inositol and (n) carnitine in both genotypes. GPC increased only in (m) C57BL/10 mice; (j) choline, (k) O-phosphocholine, and (l) glycerol were not significantly altered. (o)–(t) Amino acids: (o) glutamate, (p) aspartate, (q) 4-aminobutyrate, (r) alanine, (s) glycine, and (t) taurine. Significant differences between MDX–CLP290 and C57BL/10 vehicle groups were detected for (o) glutamate, (p) aspartate, (q) 4-aminobutyrate, (s) glycine, and (t) taurine, while (r) alanine remained unchanged. (u)–(w) Nitrogen metabolism-related metabolites: (u) adenosylhomocysteine, (v) glutamine, and (w) acetate, with no statistically significant differences. Data are presented as mean ± SEM, n = 6. Statistical significance: * $P < 0.05$; ** $P < 0.01$.

Metabolic profile of the sciatic nerve in response to CLP290 treatment

NMR analysis of sciatic nerve extracts allowed the identification of 12 polar metabolites, separated into four groups. Energy and phosphorylation (creatine, acetate, N-acetylaspartate, carnitine, and lactate)[69–73], membrane osmoregulation (choline, O-phosphocholine, and Myo-inositol)[74–77], excitatory and inhibitory amino acids (taurine, alanine, and glycine)[78], and nitrogen metabolism and methylation (formate)[79,80].

Energy and phosphorylation

After seven consecutive days of treatment with CLP290 (10 mg·kg^{-1}·d^{-1}) or β-cyclodextrin vehicle, metabolites associated with phosphorylation and energy metabolism in the sciatic nerve were quantified by NMR and expressed as nmol^{-1}·mg^{-1} of tissue (Fig. 6). Significant differences in metabolite concentrations were observed between dystrophic (MDX) and non-dystrophic (C57BL/10) mice, regardless of treatment. MDX mice consistently exhibited higher concentrations of creatine, N-acetylaspartate, carnitine, and lactate compared with C57BL/10 mice under both vehicle- and CLP290-treated conditions (* $P < 0.05$, ** $P < 0.01$, or *** $P < 0.001$; Fig. 6a, c–e). Although CLP290 treatment did not result in statistically significant changes within the C57BL/10 group, a consistent modulation of creatine, N-acetylaspartate, and lactate concentrations was observed relative to vehicle-treated controls. No apparent modulation was observed for acetate in either strain, with or without CLP290 treatment, nor for carnitine in C57BL/10 mice (Fig. 6b and d).

Osmoregulation and membranes

In parallel with these metabolic features related to energy buffering and phosphorylation, choline-related metabolites in the sciatic nerve were also quantified by NMR following the same treatment paradigm (Fig. 6). Regardless of treatment (vehicle or CLP290), MDX mice exhibited higher concentrations of choline, myo-inositol, and O-phosphocholine compared with C57BL/10 mice (** $P < 0.01$ and *** $P < 0.001$; Fig. 6f–h). Within the C57BL/10 genotype, CLP290 treatment led to increased levels of choline and O-phosphocholine, as well as a statistically significant increase in myo-inositol compared with vehicle-treated C57BL/10 mice (* $P < 0.05$; Fig. 6g). For choline, a significant difference was specifically observed between MDX mice treated with CLP290 and vehicle-treated C57BL/10 controls (** $P < 0.01$; Fig. 6f).

Excitatory and inhibitory amino acids

Considering that membrane-related metabolites and osmotic regulators are tightly linked to amino acid homeostasis and neurotransmitter pools, excitatory and inhibitory amino acid metabolites were subsequently evaluated (Fig. 6). Under vehicle-treated conditions, MDX mice exhibited significantly higher concentrations of taurine, alanine, and glycine compared with C57BL/10 mice (P ranging from < 0.01 to < 0.0001; Fig. 6i–k). CLP290 treatment did not significantly alter taurine or glycine concentrations in either genotype (Fig. 6i and k). In contrast, alanine levels were significantly modulated by CLP290 treatment in a genotype-dependent manner, with an increase observed in C57BL/10 mice and a reduction observed in MDX mice (* $P < 0.05$; Fig. 6j). Despite this modulation, alanine concentrations in MDX mice remained significantly higher than those observed in C57BL/10 mice after treatment (*** $P < 0.001$; Fig. 6j). These findings suggest that alanine may represent a metabolite sensitive to CLP290 treatment in the sciatic nerve, displaying opposite responses in dystrophic and non-dystrophic nerves.

Nitrogen metabolism and methylation

Finally, to determine whether these treatment-associated metabolic effects extended to nitrogen metabolism, formate concentrations were quantified by NMR (Fig. 6l). No statistically significant differences in formate levels were detected between C57BL/10 and MDX mice under vehicle-treated conditions, nor following CLP290 treatment. CLP290 did not modulate formate concentrations in either genotype.

Untargeted LC-MS metabolomics of the anterior tibial muscle using positive and negative ion modes

Multivariate exploratory analysis (PCA)

Principal component analysis (PCA) was applied to the LC-MS data obtained from muscle samples acquired in both positive and negative ionization modes, with the aim of exploring the global structure of the dataset prior to confirmatory statistical analyses. In both modes, BLANK samples were excluded from the PCA, in accordance with best practices in untargeted metabolomics, as they do not represent biological material, while QC samples were retained to assess analytical stability. The score plots (Supplementary Fig. S2) revealed a tendency toward separation among the experimental groups along the first two principal components, which together explained a relevant proportion of the total variance. QC samples exhibited tight and consistent clustering in the multivariate space, indicating adequate instrumental reproducibility and analytical system stability throughout data acquisition. In contrast, the biological groups displayed distinct distribution patterns, suggesting global metabolic differences associated with the MDX genotype and the experimental conditions, including the CLP condition and the administration of the biomembrane formulation (10 mg·kg^{-1}) of the CLP290 prodrug. Collectively, these results support the subsequent application of non-parametric univariate analyses and additional confirmatory statistical tests.

Non-parametric univariate statistical analysis (Kruskal–Wallis)

Based on the global structure revealed by the PCA, muscle datasets acquired in both positive and negative ionization modes were subjected to non-parametric univariate analysis using the Kruskal–Wallis test (* $P < 0.05$). This statistical approach was selected because it does not assume data normality and is appropriate for the sample size and the intensity distributions observed across the experimental groups. The analyses identified a substantial number of significantly altered features, indicating robust metabolic differences in muscle tissue detectable in both ionization modes, including 168 significant features in positive ion mode and 189 in negative ion mode. All features meeting the statistical significance criterion (* $P < 0.05$), together with their corresponding m/z values, retention times, raw P-values, and false discovery rates (FDR), are presented in Supplementary Tables S2 (positive mode) and S3 (negative mode).

Integrated visualization of metabolic alterations (Heatmap-Top 25)

In positive ion mode, PCA indicated a more heterogeneous metabolic profile, characterized by partial overlap among the experimental groups, whereas in negative ion mode, group separation was more clearly defined. In both ionization modes, non-parametric univariate analysis using the Kruskal–Wallis test identified significantly altered features, and hierarchical heatmap visualization of the 25 most significant features revealed group-dependent modulation

https://doi.org/10.48130/targetome-0026-0041

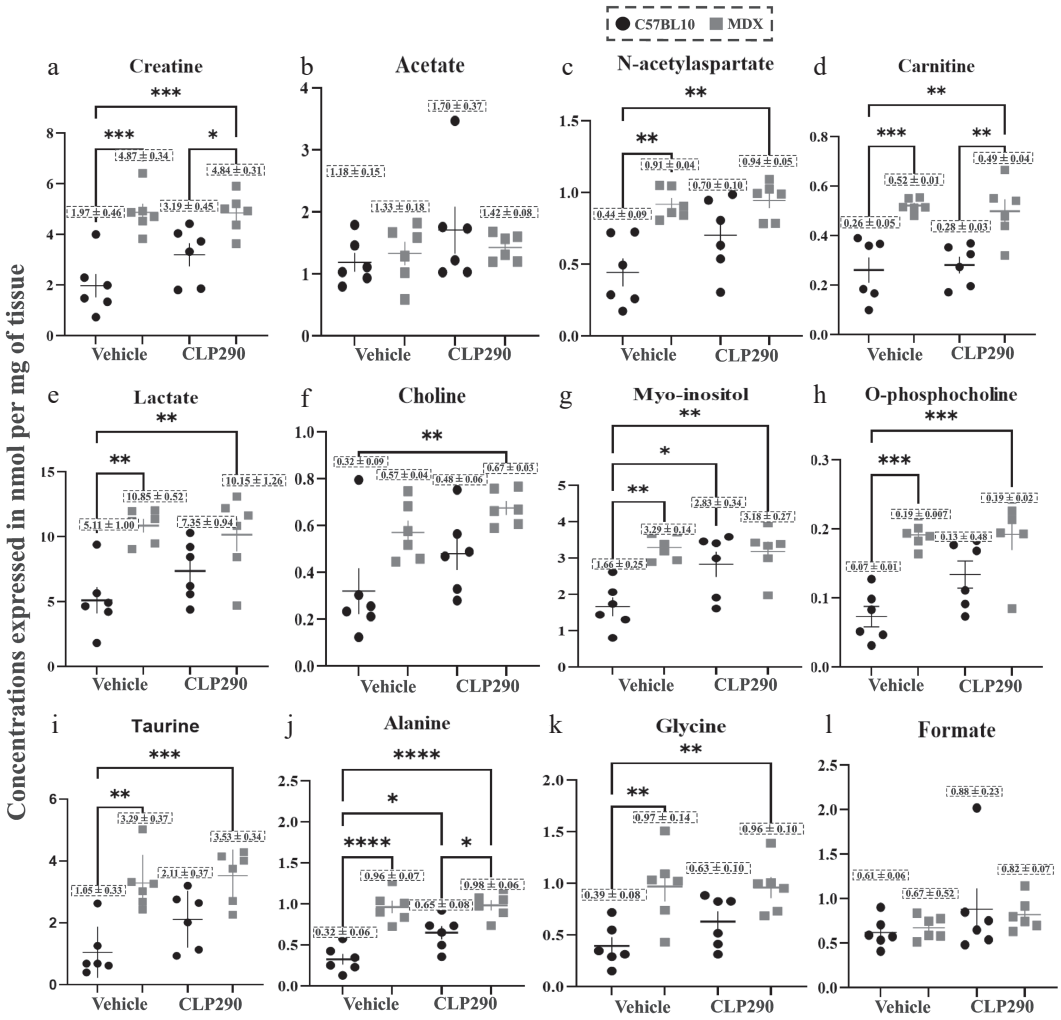

Fig. 6 Quantitative NMR-based analysis of sciatic nerve metabolites (nmol·mg^{-1} of tissue) in C57BL/10 and MDX mice treated with vehicle or CLP290 for 7 d. Energy and phosphorylation-related metabolites: (a) creatine, (b) acetate, (c) N-acetylaspartate, (d) carnitine, and (e) lactate. Significant differences between MDX and C57BL/10 mice were observed for (a) creatine, (c) N-acetylaspartate, (d) carnitine, and (e) lactate, with CLP290 reducing these differences (a), (d). No statistically significant treatment effect was detected within C57BL/10 mice, although consistent modulation of creatine, N-acetylaspartate, and lactate was observed. Acetate was not modulated: * $P < 0.05$; ** $P < 0.01$; *** $P < 0.001$. (f)–(h) Osmoregulation and membrane-related metabolites: (f) choline, (g) myo-inositol, and (h) O-phosphocholine. MDX mice exhibited higher concentrations under both conditions. CLP290 increased choline and O-phosphocholine and significantly elevated myo-inositol in C57BL/10 mice: * $P < 0.05$; ** $P < 0.01$; *** $P < 0.001$. (i)–(k) Excitatory and inhibitory amino acids: (i) taurine, (j) alanine, and (k) glycine. Under vehicle-treated conditions, MDX mice showed higher concentrations. CLP290 did not significantly affect taurine or glycine but differentially modulated alanine, increasing it in C57BL/10 mice and reducing it in MDX mice, while remaining elevated in MDX mice: * $P < 0.05$; ** $P < 0.01$; *** $P < 0.001$; **** $P < 0.0001$. (l) Nitrogen metabolism and methylation: formate concentrations showed no statistically significant differences. Data are presented as mean ± SEM, $n = 6$.

patterns. In positive mode (Supplementary Fig. S3), features with increased intensities were observed in MDX and MDXCLP samples, along with alterations associated with the CLP condition, despite greater inter-sample variability. In negative mode (Supplementary Fig. S4), abundance patterns appeared more coordinated and organized into distinct blocks, suggesting systematic rather than random metabolic alterations. Standardization of feature intensities (*z*-score) enabled relative comparisons across samples, while hierarchical clustering demonstrated greater intra-group similarity than inter-group similarity, supporting biological reproducibility. Consistent clustering of QC samples confirmed analytical stability, and QC and BLANK controls displayed predominantly low-intensity signals or values close to baseline, reinforcing data reliability and indicating that the differences observed among biological groups reflect genuine muscle-derived metabolic signals.

Univariate visualization of the most discriminative features (Boxplots-Top 6)

Based on the heatmap results, the six most significant features were selected for detailed univariate visualization using boxplots in both positive and negative ion modes (Fig. 7). These plots depict the distribution of normalized intensities [$\log_2$(Intensity + 1)] across the biological groups BL, MDX, BLCLP, and MDXCLP, enabling direct evaluation of the direction, magnitude, and dispersion of the metabolic alterations observed in muscle tissue. The boxplots revealed consistent differences between control and MDX groups, as well as additional modulation associated with the CLP290 condition, in agreement with the global results obtained from the non-parametric Kruskal–Wallis test. To complement the visual interpretation and provide statistical support, predefined pairwise comparisons were performed between the BL vs MDX and BLCLP vs MDXCLP groups using the non-parametric Wilcoxon rank-sum test, followed by

multiple-comparison adjustment with the Benjamini–Hochberg method. These comparisons were designed to capture the effect of the MDX genotype under basal conditions and under CLP290 treatment, respectively. The outcomes of the statistical tests are indicated directly on the boxplots using significance symbols, providing objective evidence for the observed group differences.

Discussion

Previous research conducted in our laboratory demonstrated a promising pharmacological alternative to suppress the development of DMD by reducing excess calcium in neuronal cells of 5-week-old MDX mice using pregabalin (PGB). Such treatment stimulated neuroprotective and pro-regenerative metabolic mechanisms in motoneurons and glial cells of MDX mice. In turn, positive results were observed on the axons, improving the myelination of Schwann cells, strengthening the cytoarchitecture of neuromuscular junctions, and protecting muscle cells. Overall, the therapy delayed the onset of motor deficits in MDX mice, observed by the evolution of motor coordination in spontaneous and forced gait tests[81,82]. In this sense, in the present investigation, we continue to search for alternative pharmacological therapies that can inhibit and control the onset of neuromuscular symptoms in 4-week-old MDX mice, a period of severe degeneration and necrosis of skeletal muscle fibers[83–89]. In this study, we used the prodrug CLP290 and observed promising pharmacological effects of the treatment, which will be detailed below, resulting in improved motor performance in MDX and C57BL/10 mice at a dose of 10 mg/kg. Possibly, the regulation of KCC2 cotransporter expression and chloride homeostasis was associated with reduced markers related to lumbar spinal cord alphamotoneurons hyperexitability[46,50]. Behaviorally, a more stable gait was obtained, leveling with C57BL/10, through dynamic/static balance, which involves reducing the base of support, and improving adduction of the hind limbs[90]. Given that, in patients with DMD and MDX mice, hip abduction and widening of the base of support occur to advance the limb in swing, and to increase postural stability[91–93]. Furthermore, CLP290-treated MDX mice achieved excellent dynamic parameters, with the maximum plantar contact area for the motor impulse against the glass platform in a step cycle[93,94]. Importantly, the present results show the downregulation of GAD65 in MDX vehicle mice, indicating weakening of GABAergic synapses, contributing to the reduction of inhibitory activity and increased motoneuron excitability[19,95,96]. Convergently, in MDX vehicle mice, we observed increased VGLUT-1 immunolabeling, which, combined with reduced chloride extrusion, reinforces the hyperexcitability hypothesis[97–99]. Increased glutamate is also related to neuroinflammatory changes and upregulation of astroglial reactivity (GFAP) in the spinal cord of MDX vehicle mice[20,100–102]. Nevertheless, compensatory mechanisms may be present regarding AMPA receptor activation, since we observed upregulated expression of AMPA receptors in the motor nucleus of MDX vehicle mice[103–105].

CLP290 treatment in MDX mice stimulated the expression of KCC2 cotransporters in the motor nucleus and plasma membrane of motor neurons, thus contributing to the reduced expression of excitatory-related molecules, such as VGLUT1 and AMPA receptors[106,107]. Overall, such balance may contribute to better cholinergic neurotransmission, seen by the increased expression of choline acetyltransferase (ChAT) observed in the plasma membrane of motoneurons in treated MDX mice[108–112]. Taken together, these synaptic and neurotransmitter-related adjustments suggest that the functional improvements observed following CLP290 treatment are associated with broader metabolic reorganization beyond synaptic modulation. Likewise, the present experimental design was not intended to establish whether the observed pharmacological effects of CLP290 are exclusively dependent on KCC2 activity. Rather, the increased membrane-associated expression of the cotransporter, together with the concomitant changes in neurotransmission-related markers, locomotor performance, and neurometabolic remodeling, supports the interpretation that the observed biological effects are consistent with KCC2-associated neuromodulation, rather than direct evidence of transporter activity. In this context, it became essential to investigate whether such functional and morphological gains were associated with central and/or peripheral metabolic adaptations, which motivated an integrated NMR-based analysis of metabolic alterations in the central and peripheral nervous systems. Accordingly, we present NMR-derived results revealing endogenous and post-CLP290 treatment metabolic alterations in the Metabolic Fundamental Axes (MFAs) of the central and peripheral nervous systems of MDX mice. To our knowledge, this is the first study to demonstrate, using NMR, that dystrophin deficiency in muscle tissue exerts retrograde and/or systemic metabolic effects on the sciatic nerve and lumbar spinal cord of these animals. We also identified metabolic signatures associated with dystrophin deficiency in the nervous system; due to their particular sensitivity, these markers may, in the future, aid in the detection of myelin alterations, the assessment of neuronal homeostasis, and the identification of energetic stress. Furthermore, metabolites from the lumbar spinal cord and sciatic nerve of 5-week-old MDX and C57BL10 mice, detected by nuclear magnetic resonance, were modulated by CLP290 (10 $mg \cdot kg^{-1} \cdot d^{-1}$) administration over 7 d of uninterrupted treatment. Metabolic results were quantified as concentrations expressed in $nmol \cdot mg^{-1}$ of tissue. Based on these measurements, CLP290 treatment was associated with selective modulation of energy metabolism, a process that plays a central role in the development and functional regulation of both the central and peripheral nervous systems[113,114]. Accordingly, the metabolic profile observed in MDX mice suggests that the most prominent metabolic alterations occurred in the spinal cord, whereas peripheral metabolic changes were comparatively modest. In the lumbar spinal cord, increased concentrations of creatine, lactate, and N-acetylaspartate were observed, concomitant with a reduction in phosphocreatine. This metabolic profile is consistent with increased utilization of phosphocreatine for the maintenance of ATP levels, reflecting a condition of elevated energetic demand and enhanced flux through the creatine-kinase system[115–118]. The creatine–kinase system plays a central role in neuronal energy homeostasis and is functionally coupled to the Na^+/K^+-ATPase, in addition to interacting with the KCC2 cotransporter[119]. Thus, intensification of this bioenergetic axis may favor KCC2 activity, contributing to the maintenance of the chloride gradient and to the stabilization of neuronal excitability, since energetic stress is known to compromise normal KCC2 function[120]. This set of alterations, observed following CLP290 treatment, is consistent with previously described mechanisms involved in the regulation of spinal cord inhibition and with reports of metabolic changes in the CNS in Duchenne muscular dystrophy, reinforcing descriptions of CNS bioenergetic dysfunction in DMD[121–123]. Although mitochondrial function was not directly assessed in this study, the metabolic profile observed in the spinal cord, particularly involving the phosphocreatine, lactate, N-acetylaspartate, and creatine pathways, is consistent with alterations in bioenergetic demand and energy metabolism associated with mitochondria[124–127]. Considering that the maintenance of chloride homeostasis through KCC2 activity requires substantial ATP consumption related to Na^+/K^+-ATPase function, it is plausible that part of the metabolic remodeling associated with CLP290 treatment may

https://doi.org/10.48130/targetome-0026-0041

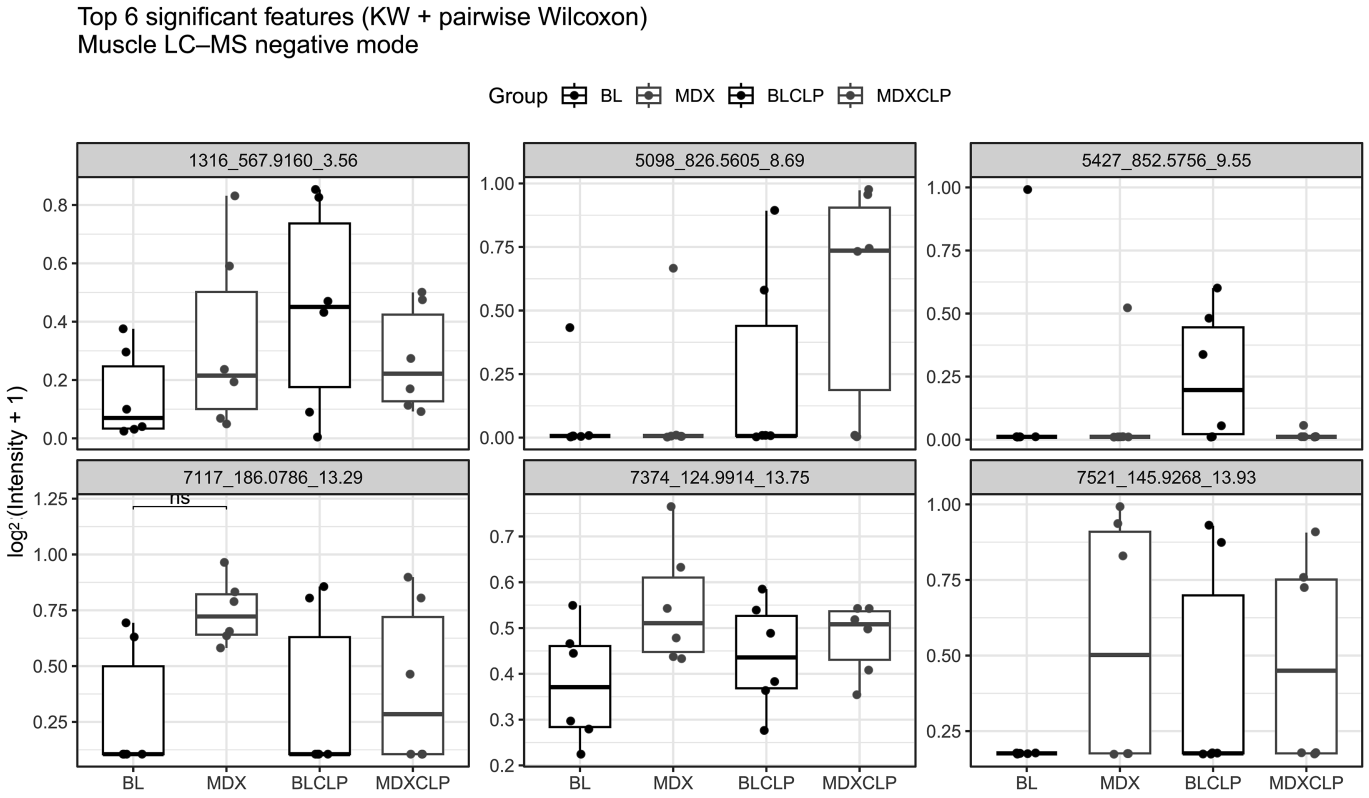

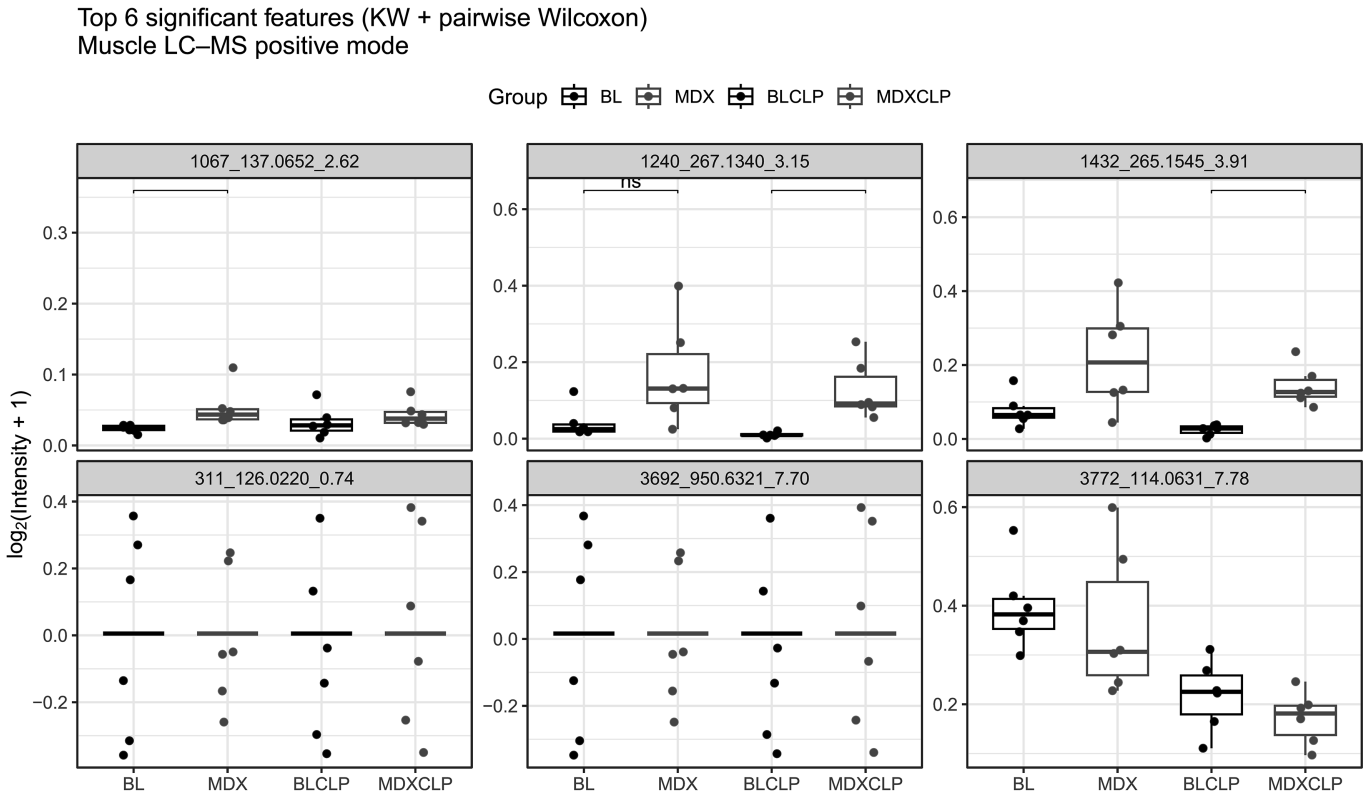

Fig. 7 Boxplots in positive and negative ion modes, respectively, show the distribution of normalized intensities [$\log_2$(intensity + 1)] for the six most significant features selected based on the Kruskal–Wallis analysis across the BL, MDX, BLCLP, and MDXCLP groups. Each panel corresponds to a specific feature (*m/z* and retention time), with individual points representing biological replicates. The plots reveal consistent differences between control and MDX muscle samples, as well as additional modulation associated with CLP290 treatment. Predefined pairwise comparisons (BL vs MDX and BLCLP vs MDXCLP) were performed using the non-parametric Wilcoxon test with Benjamini–Hochberg correction for multiple testing, and statistically significant differences are indicated directly on the boxplots.

involve indirect mitochondrial adaptations[45,128]. However, direct conclusions regarding mitochondrial function cannot be established from the present data.

Furthermore, in this study, sciatic nerve metabolites from MDX mice showed a high baseline profile of creatine, carnitine, N-acetylaspartate, and lactate, regardless of treatment. These metabolites are associated with axonal bioenergy processes and metabolic support in the nervous system, including the maintenance of nerve conduction and metabolic shielding between axons and Schwann cells[129–132]. This metabolic signature is consistent with an increased energetic burden at the axonal level, potentially associated with chronic neuromuscular degeneration[133]. The elevation of carnitine may indicate a greater reliance on lipid-related metabolic pathways, while increased lactate levels are compatible with enhanced metabolic coupling between Schwann cells and axons[134–137]. The analysis of sciatic nerve metabolites indicates that CLP290 does not normalize the elevated energetic profile characteristic of MDX mice. Despite the persistent basal elevation of creatine and carnitine in MDX nerves, CLP290 treatment did not significantly modify the concentrations of N-acetylaspartate or lactate, suggesting that axonal energetic demand and Schwann cell-associated metabolic support remain largely unchanged at the peripheral level[138]. These results suggest that the lumbar spinal cord was more responsive to metabolic modulation associated with CLP290 than peripheral tissues under the current experimental conditions, exhibiting changes in high-energy phosphate balance and glycolytic markers, whereas peripheral nerve metabolism primarily reflects sustained energy reserves and lipid-associated pathways[139]. In this context, subtle trends observed for succinate and fumarate in nervous tissue should be regarded as exploratory and interpreted with caution. Consistent with this differential central-peripheral responsiveness, the increase in myo-inositol and carnitine observed in the lumbar spinal cord, particularly in MDX mice, is compatible with enhanced osmotic regulation and increased reliance on lipid-associated energy pathways, rather than a uniform normalization of peripheral nerve metabolism[139–141]. In parallel, elevation of glycerophosphocholine (GPC) detected in CLP290-treated C57BL/10 mice suggests increased phospholipid turnover and membrane maintenance activity, consistent with adaptive remodeling of cellular membranes under pharmacological modulation[142–145]. At the peripheral level, CLP290 treatment promoted a significant increase in myo-inositol in the sciatic nerve of C57BL/10 mice, while differences in choline levels were observed in MDX animals. Together, these findings reinforce the notion that pharmacotherapy preferentially influences metabolic axes linked to osmotic balance and phospholipid dynamics, rather than directly reversing the dystrophic metabolic state in peripheral nerves[141,144,146].

Complementing these observations, MDX mice in the vehicle condition not treated with CLP290 exhibited a basal increase in myo-inositol and phosphocholine, a profile that is compatible with endogenous osmotic adaptation under chronic energetic stress, rather than an acute pharmacological effect[147,148]. Taken together, the patterns of metabolic modulation observed following CLP290 treatment across the CNS and PNS suggest that pharmacotherapy does not act through uniform normalization of individual metabolites, but rather favors the coordinated adjustment of interconnected metabolic axes, including energy/phosphorylation, osmotic regulation, and membrane-associated pathways. This central responsiveness is coupled with more limited peripheral modulation. This supports the interpretation that the metabolic effects associated with CLP290 were more pronounced in the central nervous system than in peripheral tissues, with indirect peripheral consequences, while peripheral alterations appeared secondary and comparatively less responsive under the present experimental conditions. Such a mechanism may help explain the capacity of CLP290 to support neuronal homeostasis in the context of repeated cycles of muscle degeneration and regeneration that impact the nervous system in MDX mice[134,149,150]. Within this integrative framework, balance between excitatory and inhibitory metabolites emerges as a critical component of neuronal homeostasis. Treatment with CLP290 was associated with increased concentrations of glutamate and aspartate, indicating an elevated excitatory metabolic tone. Notably, this increase occurred concomitantly with elevations in metabolites with inhibitory and modulatory functions, including GABA (4-aminobutyric acid), glycine, and taurine, particularly in the lumbar spinal cord of MDX mice. This coordinated metabolic profile is consistent with fine-tuned adjustment of excitatory-inhibitory modulation, reflecting compensatory mechanisms of neuronal stabilization rather than a state of uncontrolled excitation or excitotoxicity[151–153].

In this context, modulation of alanine, although not reaching statistical significance, may reflect its intermediary role in glutamate metabolism and in the coupling between glycolysis and the Krebs cycle, further contributing to metabolic flexibility under pharmacological intervention[154–157]. Building upon the metabolic flexibility suggested by alanine modulation, the concomitant changes observed in excitatory and inhibitory amino acid metabolites support a broader interpretation in which CLP290 may influence neuronal homeostasis through indirect regulation of ionic and metabolic coupling mechanisms. In this context, the metabolic profile observed is compatible with modulation of pathways functionally associated with KCC2 activity, rather than direct restoration of the cotransporter, potentially impacting neurotransmitter-related metabolic pools and contributing to the regulation of neuronal excitability[44,138].

At the peripheral level, elevation of taurine observed in the sciatic nerve of MDX mice following CLP290 treatment reinforces its recognized neuroprotective, osmoregulatory, and excitability-modulating roles in the peripheral nervous system[158–161].

In contrast, basal glycine concentrations in the sciatic nerve of MDX mice were not altered by treatment when compared with MDX vehicle, relative to the C57BL/10 group, suggesting that glycine may participate in peripheral inhibitory modulation in a manner less sensitive to pharmacological intervention[162,163]. Together, taurine and glycine appear to integrate indirect compensatory mechanisms involved in control of axonal excitability under dystrophic conditions, warranting further investigation[158,159,162].

In parallel, NMR analysis revealed an altered basal alanine profile in the peripheral nervous system, with higher concentrations in MDX vehicle-treated mice compared with C57BL/10 controls. This basal elevation was attenuated by CLP290 treatment in MDX mice, while alanine levels increased in treated C57BL/10 mice relative to vehicle. This bidirectional response highlights the context-dependent nature of CLP290 action, suggesting that in dystrophic nerves the drug may reduce reliance on pyruvate diversion toward alanine as a mechanism for nitrogen buffering and carbon redistribution, whereas in healthy tissue it promotes alanine accumulation, reflecting distinct metabolic adjustments according to basal energetic load[164,165]. Such differential responses are consistent with the role of monocarboxylate transport and Schwann cell-axon metabolic coupling in supporting peripheral nerve metabolism[166]. Extending this interpretation to the fourth, regulatory axis of nitrogen metabolism, treatment with CLP290 in the lumbar spinal cord was associated with increases in S-adenosylhomocysteine and acetate concentrations in MDX mice, although these changes did not reach statistical significance. This profile is compatible with partial engagement of methylation-related pathways and with modulation

of acetyl-group availability for epigenetic remodeling and energy turnover[167,168]. In parallel, glutamine concentrations exhibited a genotype-dependent response, being reduced in CLP290-treated MDX mice and increased in treated C57BL/10 mice when compared with their respective vehicle controls. This pattern suggests that the effect of CLP290 on nitrogen metabolism is modulated by the basal metabolic state of the tissue, leading to distinct adjustments in glutamine availability in dystrophic vs non-dystrophic contexts. In the sciatic nerve, no statistically significant changes were detected in nitrogen-related metabolites, indicating limited engagement of nitrogen-related metabolic pathways in the peripheral nervous system.

This observation is consistent with the broader metabolic flexibility and diversification of fluxes in the spinal cord compared with the peripheral nervous system, as discussed above. In contrast, within the peripheral nervous system, such metabolic adjustments appear secondary and less responsive. Importantly, this metabolic hierarchy, originating in the central nervous system and extending to the peripheral compartment, establishes a metabolic bridge that is reflected behaviorally and in line with the muscle metabolomics findings obtained by LC-MS. Thus, metabolomic analysis of the tibialis cranialis muscle revealed a consistent separation between MDX and BL animals in PCA analyses under both negative and positive ionization modes, indicating robust metabolic reprogramming associated with dystrophin deficiency. The greater dispersion observed in the MDX group reflects the metabolic heterogeneity typical of chronic inflammation, necrosis, and continuous muscle regeneration in early stages of the disease described in young MDX mice aged 3 to 4 weeks[166,169]. The negative ion mode highlighted alterations in polar lipids and energy metabolism, whereas the positive ion mode revealed changes in amino acids, the carnitine/acylcarnitine axis, and metabolites associated with protein turnover and oxidative stress, consistent with primary studies in the MDX model[166]. Integration of PCA, Kruskal–Wallis tests, heatmaps (Top 25), and boxplots (Top 6) confirmed that these differences do not arise from random fluctuations, but rather from structured and sustained metabolic alterations due to group differences, CLP290 treatment promoted partial displacement of the MDX metabolic profile toward the control group, with a more evident effect in the positive ion mode, suggesting modulation of metabolic pathways sensitive to the dystrophic context, possibly associated with alterations in amino acids, carnitine metabolism, and fatty acid oxidative stress[166,167]. These LC/MS findings complement the functional and NMR data, indicating that the action of CLP290 is not limited to neural modulation but also impacts muscle metabolism.

Conclusions

Taken together, the results presented here demonstrate that MDX mice, in addition to exhibiting functional impairments and immunohistochemical alterations, particularly in the ventral horn of the spinal cord involving motor nuclei, motoneuron cell bodies, and astrocytes, also display significant metabolic disturbances in the neuromuscular axis. In this context, CLP290, possibly through modulation of chloride homeostasis in motoneurons, is associated with coordinated neurometabolic modulation across the neuromuscular axis. This effect occurs predominantly at the level of the central nervous system, where treatment is associated with reduced markers related to spinal α-motoneuron hyperexcitability, improving locomotor performance. Supporting these findings, metabolic analyses by NMR and LC-MS revealed more prominent metabolic remodeling in the spinal cord, particularly in pathways related to energy metabolism, osmoregulation, neurotransmitter balance, and nitrogen metabolism, whereas peripheral metabolic alterations were comparatively less pronounced. Moreover, these central adjustments were accompanied by secondary and less pronounced metabolic responses in the peripheral nervous system and skeletal muscle, supporting a model in which functional improvement arises from systemic neural adaptation, independently of dystrophin restoration. An important limitation of the present study is the use of the classical MDX mouse model on the C57BL/10 background, which exhibits a comparatively milder phenotype than Duchenne muscular dystrophy in humans, partly due to its high regenerative capacity. Therefore, the functional and metabolic improvements observed following CLP290 treatment should be interpreted within the context of this experimental model and do not necessarily predict the magnitude of therapeutic responses in severe forms of the disease in humans. Nevertheless, even in the absence of dystrophin restoration, as observed in our Western blot analysis, the present findings suggest that modulation of mechanisms related to neuronal homeostasis and neurometabolic remodeling may contribute to delaying functional alterations associated with disease progression, postponing the onset of pathological signs and symptoms, and favoring the maintenance of mobility and quality of life. Despite these limitations, the MDX model remains widely used for investigating early pathophysiological mechanisms and neuromuscular alterations associated with dystrophin deficiency[168,169]. Taken together, these findings reinforce the translational potential of CLP290 as an adjuvant therapeutic strategy for early intervention in Duchenne muscular dystrophy.

Ethical statements

The animal experiments were approved by the Institute's Animal Use Ethics Committee (Institute of Biology—CEUA/IB/UNICAMP, protocol no. 6304–1/2023, carried out in accordance with the guidelines of the Brazilian College of Animal Experimentation (COBEA).

Author contributions

The authors confirm their contributions to the work as follows: study conception and design: Assis AD, Oliveira ALR; data collection: Assis AD, Duarte IMF; analysis and interpretation of results: Assis AD, Duarte MFI, Sussulini A, Oliveira ALR; draft manuscript preparation: Assis AD, Oliveira ALR. All authors reviewed the results and approved the final version of the manuscript.

Data availability

The datasets generated and/or analyzed during the current study are available from the corresponding author on reasonable request.

Acknowledgments

The authors would like to thank the partnership between the National Council for Scientific and Technological Development (CNPq) and the São Paulo Research Foundation (FAPESP) for the support provided under the Cooperation Agreements and the Call for Proposals for the Retention of Young Doctors-Regular Research Project. They also thank FAPESP for funding the fellowship (process no. 2023/10689-8) and the linked project (process no. 2023/01380-3, 2023/02615-4), and CNPq for supporting the Postdoctoral fellowship (process no. 151147/2023-0), as well as for additional support through the MCTI/CNPq Public Call No. 16/2024-Support for

International Scientific Research Projects (process no. 404884/2024-5). Alessandra Sussulini receives a CNPq fellowship (307153/2026-6). ALRO receives a CNPq fellowship (300429/2026-6).

Conflict of interest

The authors declare that they have no conflict of interest.

Supplementary information accompanies this paper online at: https://doi.org/10.48130/targetome-0026-0041.

Dates

Received 22 April 2026; Revised 5 August 2026; Accepted 6 August 2026; Published online 21 August 2026

References

[1] Koenig M, Hoffman EP, Bertelson CJ, Monaco AP, Feener C, et al. 1987. Complete cloning of the Duchenne muscular dystrophy (DMD) cDNA and preliminary genomic organization of the DMD gene in normal and affected individuals. *Cell* 50:509–517

[2] Özsarlak Ö, Schepens E, Parizel PM, Van Goethem JW, Vanhoenacker F, et al. 2001. Hereditary neuromuscular diseases. *European Journal of Radiology* 40:184–197

[3] Flanigan KM. 2014. Duchenne and Becker muscular dystrophies. *Neurologic Clinics* 32:671–688

[4] Orso M, Migliore A, Polistena B, Russo E, Gatto F, et al. 2023. Duchenne muscular dystrophy in Italy: a systematic review of epidemiology, quality of life, treatment adherence, and economic impact. *PLoS One* 18:e0287774

[5] Rudolfsen JH, Vissing J, Werlauff U, Olesen C, Illum N, et al. 2024. Burden of disease of Duchenne muscular dystrophy in Denmark – a national register-based study of individuals with duchenne muscular dystrophy and their closest relatives. *Journal of Neuromuscular Diseases* 11:443–457

[6] Crisafulli S, Sultana J, Fontana A, Salvo F, Messina S, et al. 2020. Global epidemiology of Duchenne muscular dystrophy: an updated systematic review and meta-analysis. *Orphanet Journal of Rare Diseases* 15:141

[7] Monaco AP, Bertelson CJ, Liechti-Gallati S, Moser H, Kunkel LM. 1988. An explanation for the phenotypic differences between patients bearing partial deletions of the DMD locus. *Genomics* 2:90–95

[8] Waite A, Tinsley CL, Locke M, Blake DJ. 2009. The neurobiology of the dystrophin-associated glycoprotein complex. *Annals of Medicine* 41:344–359

[9] Catapano F, Alkharji R, Chambers D, Singh S, Aghaeipour A, et al. 2025. A comprehensive spatiotemporal map of dystrophin isoform expression in the developing and adult human brain. *Acta Neuropathologica Communications* 13:110

[10] Aartsma-Rus A, Van Deutekom JCT, Fokkema IF, Van Ommen GJ, Den Dunnen JT. 2006. Entries in the Leiden Duchenne muscular dystrophy mutation database: an overview of mutation types and paradoxical cases that confirm the reading-frame rule. *Muscle & Nerve* 34:135–144

[11] Pearce JMS. 2005. Early observations on Duchenne-Meryon muscular dystrophy. *European Neurology* 54:46–48

[12] Whitehead NP, Yeung EW, Allen DG. 2006. Muscle damage in mdx (dystrophic) mice: role of calcium and reactive oxygen species. *Clinical and Experimental Pharmacology & Physiology* 33:657–662

[13] Duan D, Goemans N, Takeda S, Mercuri E, Aartsma-Rus A. 2021. Duchenne muscular dystrophy. *Nature Reviews Disease Primers* 7:13

[14] Dowling JJ, Weihl CC, Spencer MJ. 2021. Molecular and cellular basis of genetically inherited skeletal muscle disorders. *Nature Reviews Molecular Cell Biology* 22:713–732

[15] Nico B, Paola Nicchia G, Frigeri A, Corsi P, Mangieri D, et al. 2004. Altered blood-brain barrier development in dystrophic MDX mice. *Neuroscience* 125:921–935

[16] Pratt SJP, Shah SB, Ward CW, Kerr JP, Stains JP, et al. 2015. Recovery of altered neuromuscular junction morphology and muscle function in mdx mice after injury. *Cellular and Molecular Life Sciences* 72:153–164

[17] Banks GB, Chamberlain JS, Froehner SC. 2009. Truncated dystrophins can influence neuromuscular synapse structure. *Molecular and Cellular Neurosciences* 40:433–441

[18] Imaizumi R, Yamamoto T, Masui K, Ishigaki K, Sato T, et al. 2024. Spinal cord findings in a long-term survivor of Duchenne muscular dystrophy. *Human Pathology Reports* 37:300759

[19] Zarrouki F, Goutal S, Vacca O, Garcia L, Tournier N, et al. 2022. Abnormal expression of synaptic and extrasynaptic $GABA_A$ receptor subunits in the dystrophin-deficient *mdx* mouse. *International Journal of Molecular Sciences* 23:12617

[20] Simões GF, de Oliveira AL. 2012. Granulocyte-colony stimulating factor improves MDX mouse response to peripheral nerve injury. *PLoS One* 7:e42803

[21] Grady RM, Wozniak DF, Ohlemiller KK, Sanes JR. 2006. Cerebellar synaptic defects and abnormal motor behavior in mice lacking α- and β-dystrobrevin. *The Journal of Neuroscience* 26:2841–2851

[22] Mao Q, Ahmadi A, van Doorne L, de Vries S, Heezen L, et al. 2024. Evaluating genetic therapies targeting the central nervous system in Duchenne muscular dystrophy using high-resolution spatial transcriptomics. *Neuromuscular Disorders* 43:104441.501

[23] Prigogine C, Ruiz JM, Cebolla AM, Deconinck N, Servais L, et al. 2024. Cerebellar dysfunction in the mdx mouse model of Duchenne muscular dystrophy: an electrophysiological and behavioural study. *The European Journal of Neuroscience* 60:6470–6489

[24] Kueh SLL, Dempster J, Head SI, Morley JW. 2011. Reduced postsynaptic $GABA_A$ receptor number and enhanced gaboxadol induced change in holding currents in Purkinje cells of the dystrophin-deficient mdx mouse. *Neurobiology of Disease* 43:558–564

[25] Knuesel I, Mastrocola M, Zuellig RA, Bornhauser B, Schaub MC, et al. 1999. Altered synaptic clustering of $GABA_A$ receptors in mice lacking dystrophin (mdx mice). *The European Journal of Neuroscience* 11:4457–4462

[26] Brünig I, Suter A, Knuesel I, Lüscher B, Fritschy JM. 2002. GABAergic terminals are required for postsynaptic clustering of dystrophin but not of $GABA_A$ receptors and gephyrin. *Journal of Neuroscience* 22:4805–4813

[27] Fuenzalida M, Espinoza C, Pérez MÁ, Tapia-Rojas C, Cuitino L, et al. 2016. Wnt signaling pathway improves central inhibitory synaptic transmission in a mouse model of Duchenne muscular dystrophy. *Neurobiology of Disease* 86:109–120

[28] Sekiguchi M, Zushida K, Yoshida M, Maekawa M, Kamichi S, et al. 2009. A deficit of brain dystrophin impairs specific amygdala GABAergic transmission and enhances defensive behaviour in mice. *Brain* 132:124–135

[29] Kahle KT, Staley KJ, Nahed BV, Gamba G, Hebert SC, et al. 2008. Roles of the cation-chloride cotransporters in neurological disease. *Nature Clinical Practice Neurology* 4:490–503

[30] Pressey JC, Mahadevan V, Woodin MA. 2020. KCC2 is a hub protein that balances excitation and inhibition. *Neuronal Chloride Transporters in Health and Disease*, ed. Tang X. US: Academic Press. pp. 159–179 doi: 10.1016/B978-0-12-815318-5.00008-X

[31] Jarvis R, Ng SFJ, Nathanson AJ, Cardarelli RA, Abiraman K, et al. 2023. Direct activation of KCC2 arrests benzodiazepine refractory status epilepticus and limits the subsequent neuronal injury in mice. *Cell Reports Medicine* 4:100957

[32] Pressey JC, de Saint-Rome M, Raveendran VA, Woodin MA. 2023. Chloride transporters controlling neuronal excitability. *Physiological Reviews* 103:1095–1135

[33] Hartmann AM, Nothwang HG. 2022. NKCC1 and KCC2: structural insights into phospho-regulation. *Frontiers in Molecular Neuroscience* 15:964488

[34] Coe BP, Girirajan S, Eichler EE. 2012. The genetic variability and commonality of neurodevelopmental disease. *American Journal of Medical Genetics Part C, Seminars in Medical Genetics* 160C:118–129

[35] Cross AL, Viswanath O, Sherman AL. 2026. Pregabalin. In *StatPearls*. Treasure Island (FL): StatPearls Publishing

[36] Reznikov LR. 2017. Cystic fibrosis and the nervous system. *Chest* 151:1147–1155
[37] Mulberg AE, Wiedner EB, Bao X, Marshall J, Jefferson DM, et al. 1994. Cystic fibrosis transmembrane conductance regulator protein expression in brain. *NeuroReport* 5:1684
[38] Coull JAM, Boudreau D, Bachand K, Prescott SA, Nault F, et al. 2003. Trans-synaptic shift in anion gradient in spinal lamina I neurons as a mechanism of neuropathic pain. *Nature* 424:938–942
[39] De Luca A, Pierno S, Camerino C, Huxtable RJ, Camerino DC. 1998. Effect of taurine on excitation-contraction coupling of extensor digitorum longus muscle of dystrophic MDX mouse. In *Taurine 3*, eds Schaffer S, Lombardini JB, Huxtable RJ. Vol. 442. Boston, MA: Springer. pp. 115–119 doi: 10.1007/978-1-4899-0117-0_15
[40] Pato CN, Davis MH, Doughty MJ, Bryant SH, Gruenstein E. 1983. Increased membrane permeability to chloride in Duchenne muscular dystrophy fibroblasts and its relationship to muscle function. *Proceedings of the National Academy of Sciences of the United States of America* 80:4732–4736
[41] Kreis R, Wingeier K, Vermathen P, Giger E, Joncourt F, et al. 2011. Brain metabolite composition in relation to cognitive function and dystrophin mutations in boys with Duchenne muscular dystrophy. *NMR in Biomedicine* 24:253–262
[42] Hübner CA, Stein V, Hermans-Borgmeyer I, Meyer T, Ballanyi K, et al. 2001. Disruption of KCC2 reveals an essential role of K-Cl cotransport already in early synaptic inhibition. *Neuron* 30:515–524
[43] Coull JAM, Beggs S, Boudreau D, Boivin D, Tsuda M, et al. 2005. BDNF from microglia causes the shift in neuronal anion gradient underlying neuropathic pain. *Nature* 438:1017–1021
[44] Gagnon M, Bergeron MJ, Lavertu G, Castonguay A, Tripathy S, et al. 2013. Chloride extrusion enhancers as novel therapeutics for neurological diseases. *Nature Medicine* 19:1524–1528
[45] Doyon N, Vinay L, Prescott SA, De Koninck Y. 2016. Chloride regulation: a dynamic equilibrium crucial for synaptic inhibition. *Neuron* 89:1157–1172
[46] Rivera C, Voipio J, Payne JA, Ruusuvuori E, Lahtinen H, et al. 1999. The K^+/Cl^- co-transporter KCC2 renders GABA hyperpolarizing during neuronal maturation. *Nature* 397:251–255
[47] Markkanen M, Uvarov P, Airaksinen MS. 2008. Role of upstream stimulating factors in the transcriptional regulation of the neuron-specific K-Cl cotransporter KCC2. *Brain Research* 1236:8–15
[48] Uvarov P, Pruunsild P, Timmusk T, Airaksinen MS. 2005. Neuronal K^+/Cl^- co-transporter (KCC2) transgenes lacking neurone restrictive silencer element recapitulate CNS neurone-specific expression and developmental up-regulation of endogenous *KCC2* gene. *Journal of Neurochemistry* 95:1144–1155
[49] Karadsheh MF, Delpire E. 2001. Neuronal restrictive silencing element is found in the KCC2 gene: molecular basis for KCC2-specific expression in neurons. *Journal of Neurophysiology* 85:995–997
[50] Cai J, Wu Z, Wang G, Zhao X, Wang X, et al. 2024. The suppressive effect of the specific KCC2 modulator CLP290 on seizure in mice. *Epilepsy Research* 203:107365
[51] Mizobuti DS, Fogaça AR, Moraes FDSR, Moraes LHR, Mâncio RD, et al. 2019. Coenzyme Q10 supplementation acts as antioxidant on dystrophic muscle cells. *Cell Stress & Chaperones* 24:1175–1185
[52] Bradford MM. 1976. A rapid and sensitive method for the quantitation of microgram quantities of protein utilizing the principle of protein-dye binding. *Analytical Biochemistry* 72:248–254
[53] Mendes LF, Gaspar VM, Conde TA, Mano JF, Duarte IF. 2019. Flavonoid-mediated immunomodulation of human macrophages involves key metabolites and metabolic pathways. *Scientific Reports* 9:14906
[54] Nogueira-Ferreira R, Santos I, Ferreira R, Fontoura D, Sousa-Mendes C, et al. 2023. Exercise training impacts skeletal muscle remodelling induced by metabolic syndrome in ZSF1 rats through metabolism regulation. *Biochimica et Biophysica Acta (BBA) - Molecular Basis of Disease* 1869:166709
[55] Sander H, Wallace S, Plouse R, Tiwari S, Gomes AV. 2019. Ponceau S waste: Ponceau S staining for total protein normalization. *Analytical Biochemistry* 575:44–53
[56] Helbing DL, Böhm L, Oraha N, Stabenow LK, Cui Y. 2022. A Ponceau S staining-based dot blot assay for rapid protein quantification of biological samples. *Gels* 8:43
[57] Bear MF, Connors BW, Paradiso MA. 2020. *Neuroscience: exploring the brain*, Enhanced edition. Burlington: Jones & Bartlett Learning. 975 pp
[58] Wu D, Hersh LB. 1994. Choline acetyltransferase: celebrating its fiftieth year. *Journal of Neurochemistry* 62:1653–1663
[59] Yin X, Li J, Shin HD, Du G, Liu L, et al. 2015. Metabolic engineering in the biotechnological production of organic acids in the tricarboxylic acid cycle of microorganisms: advances and prospects. *Biotechnology Advances* 33:830–841
[60] Sato HH, Kawaguti HY. 2016. Biotechnological production of organic acids. In *Biotechnological Production of Natural Ingredients for Food Industry*. U.A.E.: Bentham Science Publishers. pp. 164–206 doi: 10.2174/97816810826531160100007
[61] Bhakoo KK, Craig T, Pearce D. 2006. N-acetylaspartate metabolism in neural cells. In *N-Acetylaspartate: A Unique Neuronal Molecule in the Central Nervous System*, eds Moffett JR, Tieman SB, Weinberger DR, Coyle JT, Namboodiri AMA. Boston, MA: Springer. pp. 27–47 doi: 10.1007/0-387-30172-0_3
[62] Coyle JT. 2006. A brief overview of N-acetylaspartate and N-acetylaspartylglutamate. *In N-Acetylaspartate: A Unique Neuronal Molecule in the Central Nervous System*, eds Moffett JR, Tieman SB, Weinberger DR, Coyle JT, Namboodiri AMA. vol 576. Boston, MA: Springer. pp. 1–6 doi: 10.1007/0-387-30172-0_1
[63] Bezerra JCB, Kemper A, Becker W. 1999. Profile of organic acid concentrations in the digestive gland and hemolymph of Biomphalaria glabrata under estivation. *Memórias do Instituto Oswaldo Cruz* 94:779–784
[64] Brosnan JT, Brosnan ME. 2013. Glutamate: a truly functional amino acid. *Amino Acids* 45:413–418
[65] Holeček M. 2023. Roles of malate and aspartate in gluconeogenesis in various physiological and pathological states. *Metabolism* 145:155614
[66] Kusukawa T, Niwa G, Sasaki T, Oosawa R, Himeno W, et al. 2013. Observation of a hydrogen-bonded 3D structure of crystalline glycerol. *Bulletin of the Chemical Society of Japan* 86:351–353
[67] Croze ML, Soulage CO. 2013. Potential role and therapeutic interests of myo-inositol in metabolic diseases. *Biochimie* 95:1811–1827
[68] Kanehisa M, Goto S. 2000. KEGG: Kyoto encyclopedia of genes and genomes. *Nucleic Acids Research* 28:27–30
[69] Wilson ADH, Hart A, Wiberg M, Terenghi G. 2010. Acetyl-L-carnitine increases nerve regeneration and target organ reinnervation - a morphological study. *Journal of Plastic, Reconstructive & Aesthetic Surgery* 63:1186–1195
[70] Ory-Lavollée L, Blakely RD, Coyle JT. 1987. Neurochemical and immunocytochemical studies on the distribution of *N*-acetyl-aspartylglutamate and *N*-acetyl-aspartate in rat spinal cord and some peripheral nervous tissues. *Journal of Neurochemistry* 48:895–899
[71] Helvacioglu F, Kandemir E, Karabacak B, Karatas I, Pecen A, et al. 2018. Effect of creatine on rat sciatic nerve injury: a comparative ultrastructural study. *Turkish Neurosurgery* 28:128–136
[72] Yao JK, Cannon KP. 1983. [^{14}]C Acetate metabolism in the peripheral nervous system. *Biochimica et Biophysica Acta (BBA) - Lipids and Lipid Metabolism* 753:331–338
[73] Rich LR, Ransom BR, Brown AM. 2022. Energy metabolism in mouse sciatic nerve a fibres during increased energy demand. *Metabolites* 12:505
[74] Padilla S, Freeman EB, Tandon P, Wilson VZ. 1993. Locally synthesized phosphatidylcholine, but not protein, undergoes rapid retrograde axonal transport in the rat sciatic nerve. *Journal of Neurochemistry* 60:1900–1905
[75] Natarajan V, Yao JK, Dyck PJ, Schmid HHO. 1982. Early stimulation of phosphatidylcholine biosynthesis during Wallerian degeneration of rat sciatic nerve. *Journal of Neurochemistry* 38:1419–1428
[76] Zhu X, Eichberg J. 1990. A myo-inositol pool utilized for phosphatidylinositol synthesis is depleted in sciatic nerve from rats with streptozotocin-induced diabetes. *Proceedings of the National Academy of Sciences of the United States of America* 87:9818–9822

[77] Mayhew JA, Gillon KRW, Hawthorne JN. 1983. Free and lipid inositol, sorbitol and sugars in sciatic nerve obtained post-mortem from diabetic patients and control subjects. *Diabetologia* 24:13–15
[78] Stevens MJ, Lattimer SA, Kamijo M, Van Huysen C, Sima AAF, et al. 1993. Osmotically-induced nerve taurine depletion and the compatible osmolyte hypothesis in experimental diabetic neuropathy in the rat. *Diabetologia* 36:608–614
[79] Ino D, Iino M. 2017. Schwann cell mitochondria as key regulators in the development and maintenance of peripheral nerve axons. *Cellular and Molecular Life Sciences* 74:827–835
[80] Brosnan ME, Brosnan JT. 2016. Formate: the neglected member of one-carbon metabolism. *Annual Review of Nutrition* 36:369–388
[81] Assis AD, Chiarotto GB, Simões GF, Oliveira ALR. 2021. Pregabalin-induced neuroprotection and gait improvement in dystrophic MDX mice. *Molecular and Cellular Neuroscience* 114:103632
[82] Assis AD, Chiarotto GB, da Silva NS, Simões GF, Oliveira ALR. 2022. Pregabalin synchronizes the regeneration of nerve and muscle fibers optimizing the gait recovery of MDX dystrophic mice. *FASEB Journal* 36:e22511
[83] Tanabe Y, Esaki K, Nomura T. 1986. Skeletal muscle pathology in X chromosome-linked muscular dystrophy (mdx) mouse. *Acta Neuropathologica* 69:91–95
[84] Lopez MA, Bontiff S, Adeyeye M, Shaibani AI, Alexander MS, et al. 2021. Mechanics of dystrophin deficient skeletal muscles in very young mice and effects of age. *American Journal of Physiology-Cell Physiology* 321:C230–C246
[85] De La Porte S, Morin S, Koenig J. 1999. Characteristics of skeletal muscle in mdx mutant mice. *International Review of Cytology* 191:99–148
[86] Ray PN, Belfall B, Duff C, Logan C, Kean V, et al. 1985. Cloning of the breakpoint of an X;21 translocation associated with Duchenne muscular dystrophy. *Nature* 318:672–675
[87] Coulton GR, Curtin NA, Morgan JE, Partridge TA. 1988. The mdx mouse skeletal muscle myopathy: II. Contractile properties. *Neuropathology and Applied Neurobiology* 14:299–314
[88] Dangain J, Vrbova G. 1984. Muscle development in mdx mutant mice. *Muscle & Nerve* 7:700–704
[89] McGeachie JK, Grounds MD, Partridge TA, Morgan JE. 1993. Age-related changes in replication of myogenic cells in mdx mice: quantitative autoradiographic studies. *Journal of the Neurological Sciences* 119:169–179
[90] Timotius IK, Roelofs RF, Richmond-Hacham B, Noldus LPJJ, von Hörsten S, et al. 2023. CatWalk XT gait parameters: a review of reported parameters in pre-clinical studies of multiple central nervous system and peripheral nervous system disease models. *Frontiers in Behavioral Neuroscience* 17:1147784
[91] D'Angelo MG, Berti M, Piccinini L, Romei M, Guglieri M, et al. 2009. Gait pattern in Duchenne muscular dystrophy. *Gait & Posture* 29:36–41
[92] Pitzer C, Kurpiers B, Eltokhi A. 2021. Gait performance of adolescent mice assessed by the CatWalk XT depends on age, strain and sex and correlates with speed and body weight. *Scientific Reports* 11:21372
[93] Garrick JM, Costa LG, Cole TB, Marsillach J. 2021. Evaluating gait and locomotion in rodents with the CatWalk. *Current Protocols* 1:e220
[94] Rizzi JS, de Barros Almeida C, Requena LS, de Almeida VD, Mininel TV, et al. 2023. Characterization of walking locomotion in aged C57BL/10 mice: a comprehensive gait analysis. *bioRxiv* Preprint:535545
[95] Fritschy JM, Schweizer C, Brünig I, Lüscher B. 2003. Pre- and post-synaptic mechanisms regulating the clustering of type A γ-aminobutyric acid receptors (GABAA receptors). *Biochemical Society Transactions* 31:889–892
[96] Vaillend C, Chaussenot R. 2017. Relationships linking emotional, motor, cognitive and GABAergic dysfunctions in dystrophin-deficient mdx mice. *Human Molecular Genetics* 26:1041–1055
[97] Yoshihara Y, Onodera H, Iinuma K, Itoyama Y. 2003. Abnormal kainic acid receptor density and reduced seizure susceptibility in dystrophin-deficient mdx mice. *Neuroscience* 117:391–395
[98] Lee HHC, Deeb TZ, Walker JA, Davies PA, Moss SJ. 2011. NMDA receptor activity downregulates KCC2 resulting in depolarizing $GABA_A$ receptor-mediated currents. *Nature Neuroscience* 14:736–743
[99] Chamma I, Heubl M, Chevy Q, Renner M, Moutkine I, et al. 2013. Activity-dependent regulation of the K/Cl transporter KCC2 membrane diffusion, clustering, and function in hippocampal neurons. *The Journal of Neuroscience* 33:15488–15503
[100] Simões GF, Oliveira ALR. 2010. Alpha motoneurone input changes in dystrophic MDX mice after sciatic nerve transection. *Neuropathology and Applied Neurobiology* 36:55–70
[101] Blasco A, Gras S, Mòdol-Caballero G, Tarabal O, Casanovas A, et al. 2020. Motoneuron deafferentation and gliosis occur in association with neuromuscular regressive changes during ageing in mice. *Journal of Cachexia, Sarcopenia and Muscle* 11:1628–1660
[102] Dowling P, Zweyer M, Sabir H, Henry M, Meleady P, et al. 2023. Mass spectrometry-based proteomic characterization of the middle-aged mouse brain for animal model research of neuromuscular diseases. *European Journal of Translational Myology* 33:11553
[103] Zhao P, Ignacio S, Beattie EC, Abood ME. 2008. Altered presymptomatic AMPA and cannabinoid receptor trafficking in motor neurons of ALS model mice: implications for excitotoxicity. *The European Journal of Neuroscience* 27:572–579
[104] Rivera-Cervantes MC, Torres JS, Feria-Velasco A, Armendariz-Borunda J, Beas-Zárate C. 2004. NMDA and AMPA receptor expression and cortical neuronal death are associated with p38 in glutamate-induced excitotoxicity *in vivo*. *Journal of Neuroscience Research* 76:678–687
[105] Satarker S, Bojja SL, Gurram PC, Mudgal J, Arora D, et al. 2022. Astrocytic glutamatergic transmission and its implications in neurodegenerative disorders. *Cells* 11:1139
[106] Gulyás AI, Sík A, Payne JA, Kaila K, Freund TF. 2001. The KCl cotransporter, KCC2, is highly expressed in the vicinity of excitatory synapses in the rat hippocampus. *The European Journal of Neuroscience* 13:2205–2217
[107] Renner M, Schweizer C, Bannai H, Triller A, Lévi S. 2012. Diffusion barriers constrain receptors at synapses. *PLoS One* 7:e43032
[108] Oda Y, Imai S, Nakanishi I, Ichikawa T, Deguchi T. 1995. Immunohistochemical study on choline acetyltransferase in the spinal cord of patients with amyotrophic lateral sclerosis. *Pathology International* 45:933–939
[109] Fu R, Tang Y, Ling ZM, Li YQ, Cheng X, et al. 2014. Lithium enhances survival and regrowth of spinal motoneurons after ventral root avulsion. *BMC Neuroscience* 15:84
[110] Peddie CJ, Keast JR. 2011. Pelvic nerve injury causes a rapid decrease in expression of choline acetyltransferase and upregulation of c-Jun and ATF-3 in a distinct population of sacral preganglionic neurons. *Frontiers in Neuroscience* 5:6
[111] Gulino R, Vicario N, Giunta MAS, Spoto G, Calabrese G, et al. 2019. Neuromuscular plasticity in a mouse neurotoxic model of spinal motoneuronal loss. *International Journal of Molecular Sciences* 20:1500
[112] Bakhit C, Armanini M, Wong WLT, Bennett GL, Wrathall JR. 1991. Increase in nerve growth factor-like immunoreactivity and decrease in choline acetyltransferase following contusive spinal cord injury. *Brain Research* 554:264–271
[113] Laughlin SB, Sejnowski TJ. 2003. Communication in neuronal networks. *Science* 301:1870–1874
[114] Buzsáki G, Kaila K, Raichle M. 2007. Inhibition and brain work. *Neuron* 56:771–783
[115] Schlattner U, Wallimann T. 2004. Metabolite channeling: creatine kinase microcompartments. In *Encyclopedia of Biological Chemistry*, eds Lennarz WJ, Lane MD. Amsterdam: Elsevier. pp. 646–651 doi: 10.1016/B0-12-443710-9/00642-6
[116] Leverve XM, Taleux N, Favier R, Batandier C, Detaille D, et al. 2007. Cellular energy metabolism and integrated oxidative phosphorylation. In *Molecular System Bioenergetics*, ed. Weinheim SV. US: Wiley. pp. 9–27 doi: 10.1002/9783527621095.ch1
[117] Vink R, Knoblach SM, Faden AI. 1987. 31P magnetic resonance spectroscopy of traumatic spinal cord injury. *Magnetic Resonance in Medicine* 5:390–394
[118] Wyss PO, Huber E, Curt A, Kollias S, Freund P, et al. 2019. MR spectroscopy of the cervical spinal cord in chronic spinal cord injury. *Radiology* 291:131–138
[119] Inoue K, Yamada J, Ueno S, Fukuda A. 2006. Brain-type creatine kinase activates neuron-specific K^+-Cl^- co-transporter KCC2. *Journal of*

Neurochemistry 96:598–608
[120] de Los Heros P, Alessi DR, Gourlay R, Campbell DG, Deak M, et al. 2014. The WNK-regulated SPAK/OSR1 kinases directly phosphorylate and inhibit the K^+-Cl^--co-transporters. *The Biochemical Journal* 458:559–573
[121] Tracey I, Dunn JF, Radda GK. 1996. Brain metabolism is abnormal in the *mdx* model of Duchenne muscular dystrophy. *Brain* 119:1039–1044
[122] Rae C, Scott RB, Thompson CH, Dixon RM, Dumughn I, et al. 1998. Brain biochemistry in Duchenne muscular dystrophy: a 1H magnetic resonance and neuropsychological study. *Journal of the Neurological Sciences* 160:148–157
[123] Mastrostefano F, Garofalo M, Nuzzo T, Bruno C, Errico F, et al. 2025. Central neurophysiological alterations in dystrophic mdx mice correlate with reduced hippocampal levels of the endogenous NMDA receptor ligand D-aspartate. *Journal of Neurochemistry* 169:e70223
[124] Pan JW, Takahashi K. 2007. Cerebral energetic effects of creatine supplementation in humans. *American Journal of Physiology Regulatory, Integrative and Comparative Physiology* 292:R1745–R1750
[125] Nelson DL, Cox MM. 2021. *Lehninger principles of biochemistry*, 8th ed. New York: W. H. Freeman
[126] Moffett JR, Ross B, Arun P, Madhavarao CN, Namboodiri AMA. 2007. N-Acetylaspartate in the CNS: from neurodiagnostics to neurobiology. *Progress in Neurobiology* 81:89–131
[127] Wallimann T, Wyss M, Brdiczka D, Nicolay K, Eppenberger HM. 1992. Intracellular compartmentation, structure and function of creatine kinase isoenzymes in tissues with high and fluctuating energy demands: the 'phosphocreatine circuit' for cellular energy homeostasis. *The Biochemical Journal* 281:21–40
[128] Kaila K, Price TJ, Payne JA, Puskarjov M, Voipio J. 2014. Cation-chloride cotransporters in neuronal development, plasticity and disease. *Nature Reviews Neuroscience* 15:637–654
[129] Lapin EP, Weissbarth S, Maker HS, Lehrer GM, Weiss C. 1983. Enzyme changes in axon, myelin, and Schwann cells in injured sciatic nerve. *Journal of Neuroscience Research* 10:9–17
[130] Deck M, Van Hameren G, Campbell G, Bernard-Marissal N, Devaux J, et al. 2022. Physiology of PNS axons relies on glycolytic metabolism in myelinating Schwann cells. *PLoS One* 17:e0272097
[131] Bais P, Beebe K, Morelli KH, Currie ME, Norberg SN, et al. 2016. Metabolite profile of a mouse model of Charcot-Marie-Tooth type 2D neuropathy: implications for disease mechanisms and interventions. *Biology Open* 5:908–920
[132] Ellegood J, McKay RT, Hanstock CC, Beaulieu C. 2007. Anisotropic diffusion of metabolites in peripheral nerve using diffusion weighted magnetic resonance spectroscopy at ultra-high field. *Journal of Magnetic Resonance* 184:20–28
[133] Wallimann T, Tokarska-Schlattner M, Schlattner U. 2011. The creatine kinase system and pleiotropic effects of creatine. *Amino Acids* 40:1271–1296
[134] Antunes-Rodrigues J, De Castro M, Elias LLK, Valença MM, McCann SM. 2004. Neuroendocrine control of body fluid metabolism. *Physiological Reviews* 84:169–208
[135] Sparkes IA. 2010. Motoring around the plant cell: insights from plant myosins. *Biochemical Society Transactions* 38:833–838
[136] Jha MK, Morrison BM. 2020. Lactate transporters mediate glia-neuron metabolic crosstalk in homeostasis and disease. *Frontiers in Cellular Neuroscience* 14:589582
[137] Kahle KT, Khanna A, Clapham DE, Woolf CJ. 2014. Therapeutic restoration of spinal inhibition *via* druggable enhancement of potassium-chloride cotransporter KCC2-mediated chloride extrusion in peripheral neuropathic pain. *JAMA Neurology* 71:640–645
[138] Fünfschilling U, Supplie LM, Mahad D, Boretius S, Saab AS, et al. 2012. Glycolytic oligodendrocytes maintain myelin and long-term axonal integrity. *Nature* 485:517–521
[139] Bremer J. 1983. Carnitine—metabolism and functions. *Physiological Reviews* 63:1420–1480
[140] Brand A, Richter-Landsberg C, Leibfritz D. 1993. Multinuclear NMR studies on the energy metabolism of glial and neuronal cells. *Developmental Neuroscience* 15:289–298
[141] Erschbamer M, Öberg J, Westman E, Sitnikov R, Olson L, et al. 2011. 1H-MRS in spinal cord injury: acute and chronic metabolite alterations in rat brain and lumbar spinal cord. *The European Journal of Neuroscience* 33:678–688
[142] Ratiney H, Sdika M, Coenradie Y, Cavassila S, van Ormondt D, et al. 2005. Time-domain semi-parametric estimation based on a metabolite basis set. *NMR in Biomedicine* 18:1–13
[143] Klein J. 2000. Membrane breakdown in acute and chronic neurodegeneration: focus on choline-containing phospholipids. *Journal of Neural Transmission* 107:1027–1063
[144] Podo F. 1999. Tumour phospholipid metabolism. *NMR in Biomedicine* 12:413–439
[145] Govindaraju V, Young K, Maudsley AA. 2000. Proton NMR chemical shifts and coupling constants for brain metabolites. *NMR in Biomedicine* 13:129–153
[146] Maki T, Liang AC, Miyamoto N, Lo EH, Arai K. 2013. Mechanisms of oligodendrocyte regeneration from ventricular-subventricular zone-derived progenitor cells in white matter diseases. *Frontiers in Cellular Neuroscience* 7:275
[147] Bouçanova F, Chrast R. 2020. Metabolic interaction between Schwann cells and axons under physiological and disease conditions. *Frontiers in Cellular Neuroscience* 14:148
[148] Bowery NG, Smart TG. 2006. GABA and glycine as neurotransmitters: a brief history. *British Journal of Pharmacology* 147:S109–S119
[149] Meldrum BS. 2000. Glutamate as a neurotransmitter in the brain: review of physiology and pathology. *The Journal of Nutrition* 130:1007S–1015S
[150] El Idrissi A, Trenkner E. 2004. Taurine as a modulator of excitatory and inhibitory neurotransmission. *Neurochemical Research* 29:189–197
[151] Cruzat V, Macedo Rogero M, Noel Keane K, Curi R, Newsholme P. 2018. Glutamine: metabolism and immune function, supplementation and clinical translation. *Nutrients* 10:1564
[152] McKenna MC, Waagepetersen HS, Schousboe A, Sonnewald U. 2006. Neuronal and astrocytic shuttle mechanisms for cytosolic-mitochondrial transfer of reducing equivalents: current evidence and pharmacological tools. *Biochemical Pharmacology* 71:399–407
[153] Newsholme P, Lima MMR, Procopio J, Pithon-Curi TC, Doi SQ, et al. 2003. Glutamine and glutamate as vital metabolites. *Brazilian Journal of Medical and Biological Research* 36:153–163
[154] Kadowaki M, Kanazawa T. 2003. Amino acids as regulators of proteolysis. *The Journal of Nutrition* 133:2052S–2056S
[155] Li K, Shi X, Luo M, Inam-U-Llah, Wu P, et al. 2019. Taurine protects against myelin damage of sciatic nerve in diabetic peripheral neuropathy rats by controlling apoptosis of Schwann cells *via* NGF/Akt/GSK3β pathway. *Experimental Cell Research* 383:111557
[156] Wu JY, Prentice H. 2010. Role of taurine in the central nervous system. *Journal of Biomedical Science* 17:S1
[157] Gruener R, Bryant HJ. 1975. Excitability modulation by taurine: action on axon membrane permeabilities. *The Journal of Pharmacology and Experimental Therapeutics* 194:514–521
[158] Natale CA, Christie MJ, Aubrey KR. 2023. Spinal glycinergic currents are reduced in a rat model of neuropathic pain following partial nerve ligation but not chronic constriction injury. *Journal of Neurophysiology* 129:333–341
[159] Wood RL, Calvo PM, McCallum WM, English AW, Alvarez FJ. 2024. GABA and glycine synaptic release on axotomized motoneuron cell bodies promotes motor axon regeneration. *bioRxiv* Preprint:623863
[160] Rojas DR, Kuner R, Agarwal N. 2019. Metabolomic signature of type 1 diabetes-induced sensory loss and nerve damage in diabetic neuropathy. *Journal of Molecular Medicine* 97:845–854
[161] Zhang Q, Song W, Liang X, Xie J, Shi Y, et al. 2020. A metabolic insight into the neuroprotective effect of Jin-Mai-Tong (JMT) decoction on diabetic rats with peripheral neuropathy using untargeted metabolomics strategy. *Frontiers in Pharmacology* 11:221
[162] Jha MK, Lee Y, Russell KA, Yang F, Dastgheyb RM, et al. 2020. Monocarboxylate transporter 1 in Schwann cells contributes to maintenance of sensory nerve myelination during aging. *Glia* 68:161–177

[163] Mentch SJ, Locasale JW. 2016. One-carbon metabolism and epigenetics: understanding the specificity. *Annals of the New York Academy of Sciences* 1363:91–98
[164] Moussaieff A, Rouleau M, Kitsberg D, Cohen M, Levy G, et al. 2015. Glycolysis-mediated changes in acetyl-CoA and histone acetylation control the early differentiation of embryonic stem cells. *Cell Metabolism* 21:392–402
[165] Joseph J, Cho DS, Doles JD. 2018. Metabolomic analyses reveal extensive progenitor cell deficiencies in a mouse model of Duchenne muscular dystrophy. *Metabolites* 8:61
[166] Khattri RB, Batra A, White Z, Hammers D, Ryan TE, et al. 2024. Comparative lipidomic and metabolomic profiling of mdx and severe mdx-apolipoprotein e-null mice. *Skeletal Muscle* 14:36
[167] Zolkipli Z, Mai L, Lamhonwah AM, Tein I. 2012. The mdx mouse as a model for carnitine deficiency in the pathogenesis of Duchenne muscular dystrophy. *Muscle & Nerve* 46:767–772
[168] Johnson EE, Ervasti JM. 2025. Stress exposure in the mdx mouse model of Duchenne muscular dystrophy provokes a widespread metabolic response. *The FEBS Journal* 292:5067–5085
[169] Stephenson KA, Xiao Q, Vaughan MB, Peters P, Denley C, et al. 2025. Neuronal hyperexcitability in dystrophin-deficient mdx hippocampal neurons: the importance of interleukin-6 and GABAergic regulation. *Scientific Reports* 15:18984